



# CHORUS

This is the accepted manuscript made available via CHORUS. The article has been published as:

## Energy-Dependent Scintillation Pulse Shape and Proportionality of Decay Components for CsI:TI: Modeling with Transport and Rate Equations

X. Lu, S. Gridin, R. T. Williams, M. R. Mayhugh, A. Gekht, A. Syntfeld-Kazuch, L. Swiderski, and M. Moszynski

Phys. Rev. Applied **7**, 014007 — Published 12 January 2017

DOI: [10.1103/PhysRevApplied.7.014007](https://doi.org/10.1103/PhysRevApplied.7.014007)

# Energy-dependent scintillation pulse shape and proportionality of decay components in CsI:Tl - modeling with transport and rate equations

X. Lu, S. Gridin, and R. T. Williams\*

*Department of Physics, Wake Forest University, Winston Salem, NC, USA*

M. R. Mayhugh

*Faceted Development, LLC, 3641 Rawnsdale Road, Shaker Hts., OH, USA*

A. Gektin

*Institute for Scintillation Materials, 60 Nauki Ave., Kharkov, Ukraine*

A. Syntfeld-Kazuch, L. Swiderski, and M. Moszynski

*National Centre for Nuclear Research, A. Soltana 7, PL-05-400 Otwock-Swierk, Poland*

(Dated: December 8, 2016)

Relatively recent experiments on the scintillation response of CsI:Tl have found that there are three main decay times of about 730 ns, 3  $\mu$ s, and 16  $\mu$ s, i.e. one more principal decay component than had been previously reported; that the pulse shape depends on gamma ray energy; and that the proportionality curves of each decay component are different, with the energy dependent light yield of the 16  $\mu$ s component appearing to be anticorrelated with that of the 0.73  $\mu$ s component at room temperature. These observations can be explained by the described model of carrier transport and recombination in a particle track. It takes into account processes of hot and thermalized carrier diffusion, electric field transport, trapping, nonlinear quenching, and radiative recombination. With one parameter set, the model reproduces multiple observables of CsI:Tl scintillation response, including the pulse shape with rise and three decay components, its energy dependence, the approximate proportionality, and the main trends in proportionality of different decay components. The model offers insights on the spatial and temporal distributions of carriers and their reactions in the track.

## I. INTRODUCTION

Ideally, spectroscopic scintillation detectors convert the energy of a particle stopped in the host into luminescence photons, whose number is proportional to the energy of the stopped particle so that the integrated luminescence (detected pulse height) depends linearly on the particle energy. In real scintillators, light emission from nonlinear interactions of carriers generated in the particle track and complexities of transport and capture along with the stochastic nature of energy deposition introduce an energy-dependent light yield, i.e. nonproportionality. This *intrinsic nonproportionality* of real materials contributes in quadrature with other factors, including absolute detected photon number and homogeneity of light collection, to determine the energy resolution [1–3]. Gamma-ray energy resolution is of practical importance for element and isotope screening in security applications, well-logging, and some medical applications as well as spectroscopy in physics experiments [4–6]. One hopes to discover and/or engineer a scintillator with both high absolute light yield and a plot of light yield versus energy (proportionality curve) that is as flat as possible.

Besides proportionality, scintillators are also characterized by measuring their pulse rise and decay times.

The rise time is important for event timing, with notable applications to time-of-flight positron-electron tomography (PET) [7] in medicine and extracting data from multiple collisions per bunch in the next-generation high-luminosity Large Hadron Collider experiments [8], for example. The decay time is important to maximum event rate with respect to pulse pile-up. The decay in different scintillators can be described as single exponential, multiple exponential, or non-exponential. In deference to the last two, one may more properly speak of the decay curve rather than decay time, including information on relative amplitudes of the decay components. It is common to refer to the *pulse shape* representing both rise and multicomponent decay. One might suppose that a single short decay would be preferred, but a multicomponent decay curve whose shape depends on ionization density enables pulse-shape discrimination between gamma-ray and massive (e.g. proton, alpha) particle events and is especially valuable for neutron and gamma discrimination in detectors. Extra information about the ionization track coded in the pulse shape could potentially improve energy resolution [9–11].

Direct experimental evidence that proportionality and pulse shape can be intertwined includes the gamma energy dependence of decay times in CsI:Tl [12] and the recent measurement of different proportionality curves for each decay time component in CsI:Tl [13]. This paper presents computational modeling aimed at duplicating the pulse shape including its energy dependence and the

---

\* williams@wfu.edu

corresponding separate proportionalities of decay components. This leads to insight on the scintillation processes involved.

The transport and rate equation model that we use to fit and analyze these experiments was used earlier to calculate proportionality of total light yield as well as time- and radial space-resolved distributions of the participating carriers and trap populations in the system of undoped CsI at two temperatures (295 and 100 K) and CsI with Tl dopant at room temperature [14]. A brief review of the model and enhancements made for the analysis in this work, primarily the reporting of scintillation pulse shape, is given in Section II. The 7-equation base model employed here is the same as the one used in Ref. [14]. There are changes in some of the material-specific rate coefficients, mainly the bimolecular recombination rate constants involving the Tl-activator in CsI:Tl ( $B_{et}$  and  $B_{tt}$ ) and the linear rate constant ( $S_{1h}$ ) for self-trapped hole capture on  $Tl^+$ .

## II. OVERVIEW OF THE MODEL

Our computational model of scintillation has been described in Ref. [14]. Starting with a specified ionization density deposited initially in a track of assumed cylindrical Gaussian profile, the recombination portion of the model calculates the fraction of this ionization that produces photon emission. The computation is performed using the coupled rate and transport equations listed in Eqs. (1-7) below, evaluated by a finite-element method. The seven equations listed below are mathematically the same as those used in Ref. [14], but we have chosen a different naming of factors comprising the coefficients of the terms involving Tl-trapped-electrons that become temporarily mobile when thermally ionized.

For reasons of computational efficiency explained in Ref. [14], we had constructed diffusion coefficient, mobility, and defect-trapping rate constant for electrons trapped in equilibrium on Tl as follows:  $D_{et} = (U_{et}/S_{1e})D_e$ ,  $\mu_{et} = (U_{et}/S_{1e})\mu_e$ , and  $K_{1et} = (U_{et}/S_{1e})K_{1e}$ , where subscript  $et$  indicates a coefficient for Tl-trapped electrons and  $e$  alone indicates corresponding coefficients for conduction electrons that have not yet entered the cycle of trapping, release, retrapping on Tl. The trapping and recapture of electrons on thallium is treated as if diffusion of  $Tl^0$  were taking place, saving the need to continue executing femtosecond time steps to deal with conduction electrons into the microsecond range where essentially all carriers are in equilibrium with traps, as will be seen in this study to be the case.  $U_{et}$  is the rate constant for untrapping an electron from  $Tl^0$  and  $S_{1e}$  is the rate constant for trapping an electron on  $Tl^+$  to form  $Tl^0$ . Thus the ratio  $(U_{et}/S_{1e})$  describes the fraction of time that an electron bound in  $Tl^0$  at thermal equilibrium spends in the conduction band, able to respond to electric fields and gradients as well as to participate as the mobile species in recombination with  $Tl^{++}$ -trapped holes or capture on other defects. In Ref. [14] we introduced  $D_{et}$ ,  $\mu_{et}$ , and  $K_{1et}$  as new material parameters even though they are scaled by the fixed ratio  $(U_{et}/S_{1e})$  relative to the free electron parameters  $D_e$ ,  $\mu_e$ , and  $K_{1e}$ . Writing the same equations now with explicit display of the ratio  $U_{et}/S_{1e} = f_e$  (for "free electron fraction") avoids the introduction of apparent new material parameters for the activator-doped material that were simply scaled from host parameters already used. For  $B_{tt}$  defined in Ref. [14] as the bimolecular rate constant for electrons from  $Tl^0$  combining with holes trapped as  $Tl^{++}$ , we introduce  $B_{tt}^0$  in the new display format where  $B_{tt} = f_e B_{tt}^0$ . The remaining symbols and terms in the equations and relevant aspects of the solution method are as described in Ref.[14].

$$\frac{dn_e}{dt} = G_e + D_e \nabla^2 n_e + \mu_e \nabla \cdot n_e \vec{E} - (K_{1e} + S_{1e})n_e - B n_e n_h - B_{ht} n_e n_{ht} - K_3 n_e n_e n_h - K_3 n_e n_e n_{ht} \quad (1)$$

$$\frac{dn_h}{dt} = G_h + D_h \nabla^2 n_h - \mu_h \nabla \cdot n_h \vec{E} - (K_{1h} + S_{1h})n_h - B n_e n_h - B_{et} n_{et} (1 - f_e) n_h - K_3 n_e n_e n_h - K_3 n_e n_{et} n_h \quad (2)$$

$$\frac{dN}{dt} = G_E + D_E \nabla^2 N - (S_{1E} + K_{1E})N - R_{1E}N + B n_e n_h - K_{2E} N^2 \quad (3)$$

$$\frac{dn_{et}}{dt} = D_e \nabla^2 n_{et} f_e + \mu_e \nabla \cdot n_{et} f_e \vec{E} + S_{1e} n_e - K_{1e} n_{et} f_e - B_{et} n_{et} (1 - f_e) n_h - B_{tt}^0 n_{et} f_e n_{ht} - K_3 n_e n_{et} n_h \quad (4)$$

$$\frac{dn_{ht}}{dt} = D_{ht} \nabla^2 n_{ht} - \mu_{ht} \nabla \cdot n_{ht} \vec{E} + S_{1h} n_h - K_{1ht} n_{ht} - B_{ht} n_e n_{ht} - B_{tt}^0 n_{et} f_e n_{ht} - K_3 n_e n_e n_{ht} \quad (5)$$

$$\frac{dN_t}{dt} = S_{1E} N - R_{1Et} N_t + B_{ht} n_e n_{ht} + B_{et} n_{et} (1 - f_e) n_h + B_{tt}^0 n_{et} f_e n_{ht} - K_{2Et} N_t^2 \quad (6)$$

$$S_{1x} = \frac{n_{Tl^+}}{n_{Tl^+}^0} S_{1x}^0, \quad \text{where} \quad n_{Tl^+} = n_{Tl^+}^0 - n_{et} - n_{ht} - N_t \quad (7)$$

The radiative rates,  $R_{1Et} N_t$  from excited  $Tl^{+*}$  and  $R_{1E} N$  from STE are evaluated from solution of the cou-

pled equations for all populations as a function of time

starting from an initial on-axis excitation density  $n_0$ . The time-integrated radiative rate gives the corresponding light output. Division of the total light output by the total number of initial electron-hole pairs at the initial excitation density being considered gives light yield as a function of the initial ionization density. We call this intermediate result the Local Light Yield,  $Y_L(n_0)$ . The calculation is repeated for a number of excitation densities.

In the energy deposition part of the model calculation, GEANT4 Monte Carlo simulations [15] are used to record the energy and track length for each sub event making up the total deposition by a mono-energetic electron of initial energy  $E_i$ . From such simulations, the ionization density (e-h/cm<sup>3</sup>) can be determined for every parcel of energy deposited based on the  $dE/dx$  so calculated and the assumed Gaussian radial profile of the track having initial radius  $r_0$ , which is a parameter of the model. The calculations of Local Light Yield are carried out for a range of ionization densities that span the GEANT4 results.

Introduction of a radial profile of some kind is essential on dimensional grounds to convert the rate of linear energy deposition  $dE/dx$  (eV/nm) to units of deposited carrier density (e-h/cm<sup>3</sup>) in terms of which the kinetic rate and transport equations are defined. The conversion is written as:

$$n_0 = \frac{dE/dx}{\pi r_0^2 \beta E_{gap}}, \quad (8)$$

where  $r_0$  is the  $1/e$  radius of the track profile expressed as  $\exp(-r^2/r_0^2)$  in Ref. [16] and  $\beta E_{gap}$  is the average energy invested per electron-hole pair created. Using this conversion and the GEANT4 simulations yields a probability of occurrence of each excitation density  $n_0$  during the stopping of a primary electron of initial energy  $E_i$ , written as  $F(n_0, E_i)$ . In the calculations of Ref. [14], an average probability function  $F_{av}(n_0, E_i)$  was constructed from 100 to 2000 GEANT4 simulations at each initial electron energy, whereas in the present work the single-simulation probability function  $F(n_0, E_i)$  is used to calculate and store 100 to 2000 light yields of simulated single events, which can be averaged at the end. Given the same set of simulated events the averaged light yield results are the same for either method. The approach adopted here is well suited for the simulation and analysis of pulse height spectra in future work.

Having both  $F(n_0, E_i)$  from GEANT4 simulations and the local light yield  $Y_L(n_0)$  from the solution of Eqs (1-7), the formal calculation of light yield as a function of initial energy (i.e. electron response or proportionality) is obtained by integrating the product  $F(n_0, E_i)Y_L(n_0)$  over  $n_0$ . We have used an interpolation procedure in this step. Fifteen or so local light yield calculations,  $Y_L(n_0)$ , were used as a framework to interpolate the light response for each parcel of excitation density, and the contributions

from all such parcels were summed to give the scintillator's response to that electron.

For the study of rise and decay times in this work, the  $Y_L(n_0)$  values are recorded for all excitation densities at times of interest during the initial calculation. Subsequently the response at each time can be calculated. Repeating the process at various times gives the signal as a function of time for the initial electron energy under consideration. Completing the calculation for all modeled energies gives the pulse shape for each energy and proportionality as a function of time.

In Eq.(6) above, the population of excited activator,  $Tl^{+*}$ , is denoted by  $N_t$  meaning "exciton trapped on activator". Similarly, the density of self-trapped holes [STH] is  $n_h$ , and the density of thallium-bound electrons [ $Tl^0$ ] is  $n_{et}$ . The term  $B_{et}n_{et}(1-f_e)n_h$  ( $\approx B_{et}n_{et}n_h$ ) governs the moderately fast bimolecular formation of  $Tl^{+*}$  by the well-known reaction  $STH + Tl^0 \rightarrow Tl^{+*}$ . The  $B_{tt}^0 n_{et} f_e n_{ht}$  term governs the slower process involving trapped electron release from  $Tl^0$  followed by capture of the electron on  $Tl^{++}$  that had been formed by prior hole capture (at the rate  $S_{1h}n_h$ ), to also produce excited activator,  $Tl^{+*}$ . The following sections will refer especially to the three parameters,  $B_{et}$ ,  $B_{tt}^0$  and  $S_{1h}$ , which have critical roles in determining the pulse shape in CsI:Tl. Thus fitting pulse shape presents an opportunity to refine their values before addressing proportionality and total light yield.

The model of Ref. [14] was developed and tested for electron proportionality (relative light yield versus electron energy), and is used in the present work to compare with gamma-ray proportionality data [12, 13]. Swiderski et al [17] have compared electron response and gamma response of CsI:Tl from about 30 keV to 1 MeV. With a 12  $\mu$ s shaping time, the differences between gamma and electron response over this energy range were modest, so we believe the comparisons being made in the present work are informative and support useful conclusions about mechanisms of both electron and gamma response. In forthcoming work we will model gamma proportionality and pulse height spectrum directly.

### III. PULSE SHAPE AND ITS ENERGY DEPENDENCE

#### A. Experimental data

Syntfeld-Kazuch et al [12] measured pulse shape of CsI:Tl (0.06%) excited at several gamma-ray energies between 662 keV and 6 keV using a so called slow-slow single-photon method described in Refs [18] and [19], tailored to reduce the background of random coincidences. With this method they were able to resolve a "tail" decay component of about 16  $\mu$ s in addition to the "fast" and "slow" components of 730 ns and 3.1  $\mu$ s reported in prior studies of CsI:Tl scintillation decay [20, 21]. The pulse shapes for 662 keV and 6 keV gamma excitation measured in Ref. [12] are plotted in Fig. 1. The 16  $\mu$ s tail

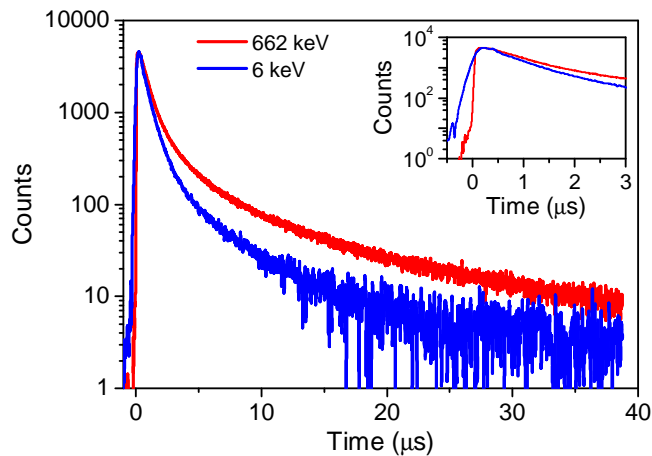


FIG. 1. Experimental pulse rise and decay over the full measured range 0 to 40  $\mu\text{s}$  in CsI:Tl from Ref. [12] is shown for 662 keV gamma excitation in the red trace and for 6 keV gamma excitation in the lower blue trace.

accounts for about 22% of the integrated pulse for 662 keV excitation, compared to 48% and 30% for the fast and slow components respectively [12]. Decay curves of scintillation from 16.6, 60, 122, and 320 keV gamma rays were also measured in Ref. [12], reported in terms of fitted exponentials and their amplitudes.

The decay times of  $730 \pm 30$  ns,  $3.1 \pm 0.2 \mu\text{s}$ , and  $16 \pm 1 \mu\text{s}$  were determined by fitting the decay curve for 662 keV excitation [12]. The corresponding decay times under 6 keV excitation were  $670 \pm 20$  ns,  $3.1 \pm 0.3 \mu\text{s}$  and  $14 \pm 3 \mu\text{s}$ , indicating that the fast and tail decay times decrease slightly with decreasing gamma energy. Noting that there is only a weak dependence of the fitted decay times upon gamma ray energy, the authors of Ref. [12] presented data on how the relative amplitudes (integrated intensities) of the fast, slow, and tail decay components changed in six gamma energy steps from 662-keV to 6-keV. A main conclusion of their study was that the fast/tail ratio increases as gamma excitation energy is lowered. Fitting the observed pulse shape as a function of energy and understanding the physical origins of the decay components are among our objectives in this work.

The data in Fig. 1 are a multichannel analyzer record of times from start to single photon stop events which samples the scintillation lifetime and is adjusted with delays to put the start-time for the pulse on scale. This means that the data records shown in Fig. 1 show the rising portion of the curve within the stated 20-ns experimental resolution in Ref.[12]. However, the measurement method itself does not specify a time zero. The rise to a peak and initial decay out to  $2.5 \mu\text{s}$  are shown on an expanded time scale in the inset of Fig. 1. Syntfeld-Kazuch et al normalized their data at the peak for display and we will follow their lead in making comparisons to the model. The time zero in the model is definite, corresponding to the initial energy deposition, and can be read from the

model curve matched to the experiment curve at its peak. The curves in both the main figure and the inset of Fig. 1 are normalized and presented with the peak intensities coinciding in time and amplitude. The red and blue traces in the inset are for 662 keV and 6 keV excitation measured by Syntfeld-Kazuch et al in an experiment optimized for weak signals at long times [12, 18, 19]. We have also examined 511 keV excitation data measured by Valentine et al [20] in an experiment optimized for fast response at expense of resolving slow, weak signals.

Many previous studies [20–23] have associated the  $\sim 700$  ns fast decay mainly with the reaction  $\text{STH} + \text{Tl}^0$ , and the  $\sim 3 \mu\text{s}$  slow decay with electrons thermally released from  $\text{Tl}^0$  recombining with  $\text{Tl}^{++}$  that were formed by STH capture at  $\text{Tl}^+$  dopants. This association of the two main physical recombination routes involving STH and  $\text{Tl}^{++}$  respectively with the decay components seemed complete when there were only two decay components known experimentally (other than what was considered afterglow). With three identifiable decay components having roughly similar integrated strengths now known [12], an assessment of the responsible physical mechanisms seems in order.

Our underlying model accounts for trapping of both electrons and holes by  $\text{Tl}^+$  in the lattice. Carriers created by high-energy radiation are initially hot, with excess kinetic energy. As a result, electrons created in CsI spread quickly to a mean radius of about 50 nm (extending as far as 200 nm) [24], and are trapped with a  $1/e$  time of  $\sim 3$  ps [14, 25] by  $\text{Tl}^+$  to form  $\text{Tl}^0$ . Self-trapping of the co-produced holes is commonly presumed to localize them initially at the original track. The transport and recombination kinetics of these self-trapped holes (STH) with the  $\text{Tl}$ -trapped electrons (denoted  $\text{Tl}^0$ ) initially governs the formation of excited  $\text{Tl}^{+*}$  that are responsible for scintillation light. Together with the  $\text{Tl}^{+*}$  photoluminescence decay time of 575 ns, these transport and recombination kinetics determine the finite rise time and the 730-ns fast decay time of scintillation in CsI:Tl. In parallel, the STH are competitively trapped on  $\text{Tl}^+$ , accumulating a population of  $\text{Tl}$ -trapped holes ( $\text{Tl}^{++}$ ) until all STH are exhausted by these two channels. With appropriate proximity and thermal untrapping of electrons from  $\text{Tl}^0$ , this  $\text{Tl}^{++}$  population, considered deeply trapped and immobile, recombines with the electrons released from  $\text{Tl}^0$  to produce  $\text{Tl}^{+*}$  at longer times. For these calculations we adopt the conventional assumption that it is the electron that is untrapping from  $\text{Tl}^0$ . An alternative suggestion that  $\text{Tl}^0$  is a deep electron trap [26–28] and instead holes untrap thermally from  $\text{Tl}^{++}$  to recombine with the static  $\text{Tl}^0$  has been made [26].

## B. Model results – Fitting rise and decay times

The 662 keV pulse shape data reported in Ref. [12] is reproduced by the red trace with noise in Fig. 2(a,b). The smooth curve superimposed shows the simulation

of  $\text{Tl}^{+*}$  emission calculated by the model described in Section II with material input parameters to be tabulated and discussed later in this paper.

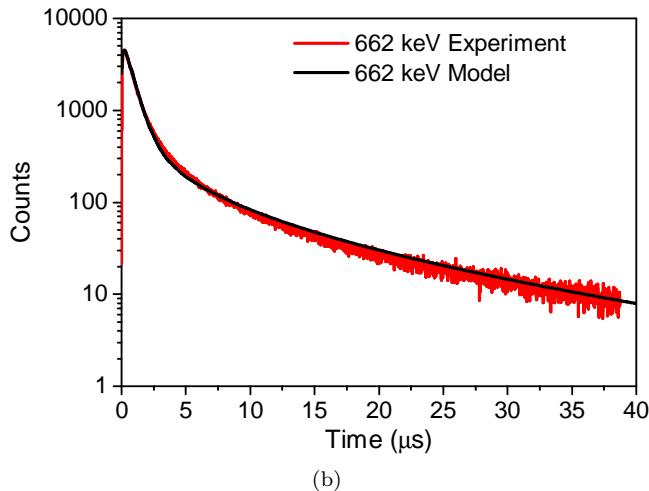
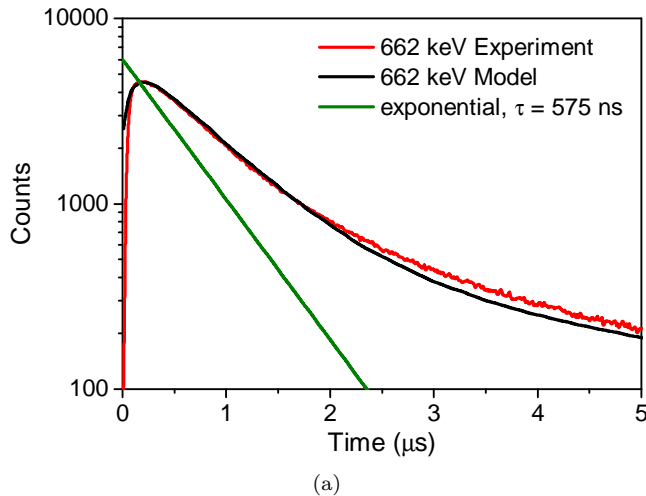


FIG. 2. Experimental scintillation decay curve from Ref. [12] for 662 keV gamma excitation shown in red trace with noise on (a) 0 to 5  $\mu\text{s}$  time scale and (b) 0 to 40  $\mu\text{s}$  scale. In both cases the superimposed smooth black line is the modeled light output for 662 keV excitation. Model is normalized to experiment at the peak.

The experimental data and model calculation for 662 keV excitation are shown on a log scale versus linear time out to 5 microseconds in Fig. 2(a). Superimposed is a 575 ns exponential representing the decay time measured for uv-excited  $\text{Tl}^{+*}$  photoluminescence in CsI:Tl at room temperature by Hamada et al [21]. It has been shown that Tl photoluminescence in CsI exhibits 4 bands, and the dominant visible luminescence at room temperature (2.25 eV) has been attributed to an STE perturbed by substitutional  $\text{Tl}^+$  on an adjacent site [29]. In the present modeling at room temperature, we have approximated it simply as one excited state with 575 ns photoluminescence decay time, called by the short name  $\text{Tl}^{+*}$ . Future

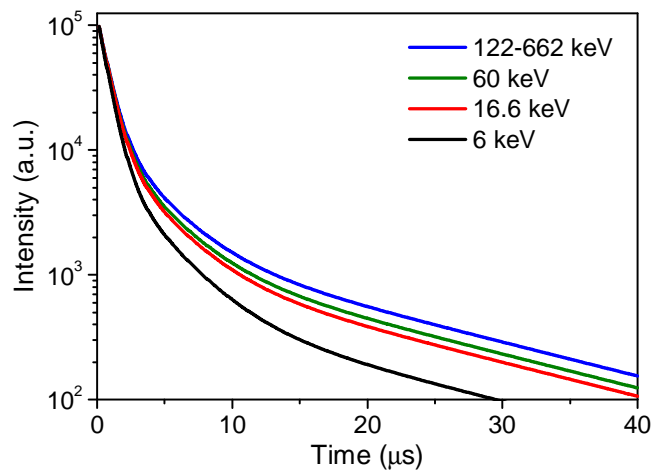


FIG. 3. Reconstructions of measured scintillation decay curves for 6 gamma-ray energies in CsI:Tl(0.06%) based on the time constants and integrated amplitudes reported in Ref. [12]. Only the decay curves are represented. The curves for 122, 320, and 662 keV overlap in the top curve.

studies may examine whether the complexity of the Tl emission center itself further complicates the scintillation decay, such as how the various energy minima of the excited state are populated in the scintillation process. The observed scintillation decay is slower than 575 ns, as can be seen in the figure and as many others have observed. As discussed by previous authors [20–22, 30], the main mechanism for formation of  $\text{Tl}^{+*}$  in the first 200 ns or so is the hopping diffusion and capture of self-trapped holes (STH) on  $\text{Tl}^0$  sites formed much earlier by rapid electron capture on  $\text{Tl}^+$ . For the scintillation decay to be longer than the 575 ns photoluminescence decay time, the excited Tl population should be fed while it also undergoes radiative decay. This formation process also accounts for the initial rise characteristics.

In part (b) of Fig. 2, the model calculation with the same parameters is compared to the full range of the experimental 662 keV scintillation decay out to 40  $\mu\text{s}$ . In Ref. [12], raw data with noise and the rise to a peak before decay were shown only for the 662 and 6 keV gamma energies. However, decay data for six gamma energies of 662, 350, 122, 60, 16.6, and 6 keV were reported as a set of three fitted exponential decay times and the amplitude of each [12]. We have reconstructed the decay curves shown in Fig. 3 from the experimentally determined decay constants and amplitudes reported in Ref. [12]. The experimental curves for 662, 350, and 122 keV overlap, so what is seen in Fig. 3 is a single curve labeled 122-662 keV at the top, with three curves below it for 60, 16.6, and 6 keV respectively. There is no representation of the early rise to a peak. These reconstructed decay curves are normalized to a value  $10^5$  at  $t = 150$  ns, which corresponds to the peak of the intensity curve in the model results.

The modeled light output curves are shown in Fig. 4

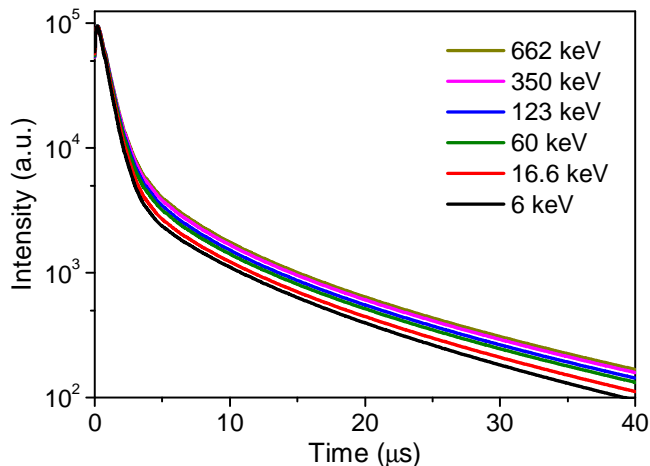


FIG. 4. Decay curves calculated from the model for six electron energies of the same values as the gamma energies of the reconstructed experimental decay curves in Fig. 3.

for gamma energies of 662, 350, 122, 60, 16.6, and 6 keV. The curves are normalized to  $10^5$  at 150 ns, the peak of light output. We did not display all of the experimental and modeled curves in a single figure because it would be hard to distinguish them. Except for the 6 keV curve, the pulse shape is similar in model and experiment. As will be discussed in Section VII, we did not try to do an exact fit with many free parameters, but revised as few material input parameters as possible relative to Ref. [14]. As a result some of the remaining differences between Figs. 3 and 4 are probably attributable to input parameter values that are not yet fully correct, though deficiencies in the model itself cannot be ruled out. For example the experimental curves in Fig. 3 are more rounded in the range of 3 - 5  $\mu$ s than are the simulated curves of Fig. 4. The common trend of increasing peak/tail ratio with decreasing energy is displayed in both simulation and experiment.

There is disagreement in the amount of tail amplitude change (relative to the peak of the fast component amplitude) between model and experiment at the lowest excitation energy, 6 keV. In the model, the depression of the relative tail amplitude continues at a rate consistent with the trend at higher energies, but the tail amplitude in experiment drops a great deal more from 16.6 to 6 keV than at any other energy intervals, and thus differs from the model. One possible reason for the disagreement between experiment and model at very low gamma energy is a known difficulty of light yield and decay time studies when the excitation occurs near the surface. A 6-keV gamma- or x-ray has an attenuation length of about 3.6  $\mu$ m in CsI. This is within the range of the surface in which quenching effects have often been reported [31, 32]. Such effects could be expected to affect the long tail of excitation decay more severely than the fast component because a longer time interval allows more diffusion toward the surface and quenching to oc-

cur. The amplitude of the tail could be decreased and its apparent decay time shortened because of the competing channel for de-excitation presented by quenching centers near the surface.

The model curves shown in Fig. 2 reach a peak at about 200 ns, matching the measurements in Ref. [33] which used methods chosen to reduce random coincidences [19] at some sacrifice of rise time resolution. Rise and peaking data for CsI:Tl were reported by Valentine et al. with better time resolution [20]. Their data include an ultrafast component that can be aligned with the rise of the calculated STE emission in the model curve. Comparison on that basis indicates that the experiment reaches its peak 50 to 100 ns sooner than the results fitted to the Syntfeld-Kazuch et al measurement [12]. Hamada et al. report decay data that for samples with Tl content from  $10^{-6}$  to  $10^{-2}$  and their rise time ranges from 100 to 185 ns. As commented earlier, these alternate fast-time data sets do not include decay data to long times (20-40  $\mu$ s), so we have concentrated on fitting the full set of data from Syntfeld-Kazuch et al [12]. The contribution of STE luminescence is not plotted in Fig 2. The STE contribution to luminescence at room temperature is very small compared to the  $Tl^{+*}$  emission except in details of the initial rise that occur within the 20-ns resolution of the experimental data now being compared. It is known from experiment that the STE in CsI at room temperature is thermally quenched to about 2% yield coming as 15 ns emission from an equilibrated Type I/Type II STE configuration [32].

#### IV. NONPROPORTIONALITY OF EACH DECAY COMPONENT – EXPERIMENTAL DATA AND MODEL RESULTS

The proportionality curves for the fast, tail, and total decay components in CsI:Tl(0.06%) were reported by Syntfeld-Kazuch et al [13] in 2014, following the method developed in Ref. [34] and are replotted below in Fig. 5(a). The experimental proportionality curves for decay components in Fig. 5(a) were determined by fitting the measured decay curve at each gamma energy to 730 ns, 3  $\mu$ s, and 16  $\mu$ s components and plotting the integrated light yield in each component versus gamma energy, normalized at 662 keV.

Figure 5(b) plots the calculated proportionality curves for the fast (730 ns) and tail (16  $\mu$ s) components as well as the total pulse proportionality in CsI:Tl(0.06%) using the model of Eqs. (1-7) [14] and the same parameters that produced the preceding fits of the pulse shape data. To emphasize, the calculated proportionality curves in Fig. 5(b) came directly out of the model with its parameter set refined to give good fits to the rise and decay data, without any further fitting to reproduce the proportionality curves of separate decay components.

The approximate proportionality curves for specified decay times in Fig. 5(b) were calculated from the model



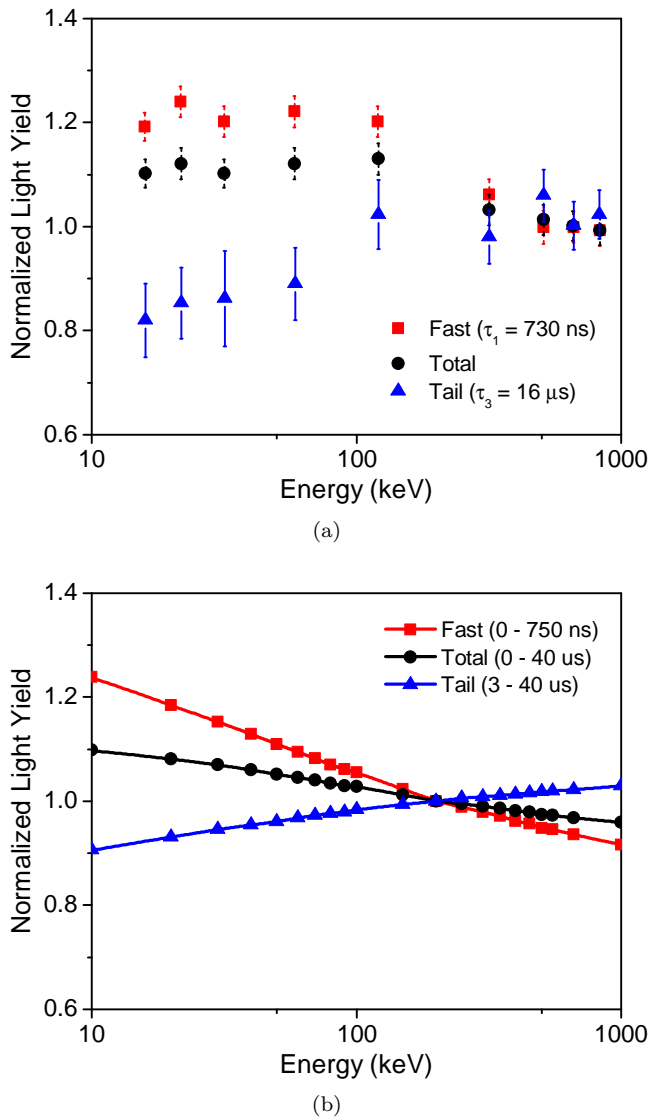


FIG. 5. (a) Experimental proportionality curves for the fast ( $0.73 \mu\text{s}$ ) and tail ( $16 \mu\text{s}$ ) decay components as well as the proportionality of total emission (Fast + Slow ( $\tau_2 = 3 \mu\text{s}$ ) + Tail) in CsI:Tl are plotted versus gamma ray energy. Reproduced from Ref. [13]. (b) Simulated proportionality curves for fast, total, and tail decay components in CsI:Tl calculated with the same model and parameter set used for Fig. 2 and Fig. 4. The integration gate intervals for Fast, Total, and Tail are given in the legend. Model curves are normalized at 200 keV for reasons discussed in Ref. [14].

output in the following way. The integrated light emission from 0 to 750 ns was plotted as "fast" light yield versus electron energy; from 750 ns to 3  $\mu$ s as "slow" light yield versus energy; from 3  $\mu$ s to 40  $\mu$ s as "tail" light yield versus energy; and 0 to 40  $\mu$ s as the total light yield versus energy. We are comparing proportionalities of decay components calculated by a simulated gating time method with experimental proportionalities of decay components analyzed as integrated strengths of three fitted exponential components. There should be qualita-

tive and reasonable quantitative correspondence between the two methods. Qualitative correspondence is what we are pointing out in Fig. 5. The modeled proportionality curves were normalized at 200 keV for reason discussed in Ref. [14]. It is a consequence of the approximate energy range over which the cylinder approximation of the track is valid.

## V. ORIGIN OF THREE DECAY COMPONENTS OF SCINTILLATION IN CSI:Tl

Two particularly intriguing questions are posed by the experimental observations reviewed in Sections III.A and IV: (a) To what can the three main decay components of  $0.73 \mu\text{s}$ ,  $3.1 \mu\text{s}$ , and  $16 \mu\text{s}$  in CsI:Tl be attributed? (b) To what can the different proportionality curves for the three decay components, particularly the anticorrelation of fast and tail components, be attributed? We address the origin of the three decay times first.

### A. Recombination reactions resulting in $Tl^{++}$ light emission in CsI:Tl

Beginning with Dietrich and Murray [22] and in many works since [20, 23], four main recombination processes have been considered to contribute to CsI:Tl scintillation. Reaction #1 comprises direct  $Tl^+$  excitation and/or prompt electron and free hole capture on  $Tl^+$  to contribute a promptly rising signal that should decay at the 575 ns photoluminescence decay time of  $Tl^{++}$ . However this pure 575 ns decay is rarely distinguishable against the stronger 730 ns "fast component" of CsI:Tl scintillation commonly attributed to Reaction #2 – self-trapped holes recombining with electrons on  $Tl^0$ ,  $STH + Tl^0 \rightarrow Tl^{++}$ . Reactions #1 and #2 together should contribute to the observed fast scintillation decay, with R#2 dominant, because self-trapping of holes is very fast, and hot electrons disperse and form  $Tl^0$  mostly separated from the STH in the track core.

As reviewed in the Introduction and elsewhere [14, 20–23, 35] the generally accepted Reaction #3 in CsI:Tl is the thermal release of electrons trapped early in the track formation as  $Tl^0$ , followed by diffusion through repeated release and recapture until recombination with a hole trapped as  $Tl^{++}$ . For a shorthand label, we write this as reaction #3:  $Tl^0 + Tl^{++} \rightarrow Tl^{++}$ . This reaction has been considered responsible for the single observed slow component of roughly 3  $\mu$ s seen in works prior to Ref. [12], e.g. as reviewed by Valentine et al [20]. Kerisit et al noted that the 3- $\mu$ s time range brackets the decay time of  $Tl^0$  due to electron release at room temperature,  $\sim 1.8 \mu\text{s}$  [36], and associated the single time constant  $\tau_e$  (for electron release from  $Tl^0$ ) with the scintillation decay time of approximately 3  $\mu$ s [23].

Reaction #4 involving Tl in alkali halide scintillators is  $STE + Tl^+ \rightarrow Tl^{++}$ , i.e. self-trapped excitons mi-



grating to encounter substitutional  $\text{Tl}^+$  and transferring their excitation to create  $\text{Tl}^{+*}$ . Murray and Meyer in 1961 [35] suggested this STE reaction channel as having main responsibility for scintillation in  $\text{NaI:Tl}$ . However, following subsequent time-resolved kinetic studies on  $\text{KI:Tl}$  with partial extension to  $\text{NaI:Tl}$ , Dietrich et al concluded in 1973 that "... nearly all ( $\approx 95\%$ ) of the energy transport takes place by electron-hole diffusion." [22]. The computational model used herein takes into account very rapid spatial separation of hot electrons relative to self-trapped holes [24] and the effect of rapid electron trapping on  $\text{Tl}^+$  directly measured by ps spectroscopy [25]. These effects hinder the formation of STEs in  $\text{Tl}$ -doped  $\text{CsI}$ , relative to undoped  $\text{CsI}$  where the line of holes draws free conduction electrons back to the track after they thermalize [14]. STEs that form in  $\text{CsI:Tl}$  despite the fast competing channels of carrier capture on  $\text{Tl}$  must then survive thermal quenching at room temperature [32] in order to finally excite  $\text{Tl}^+$ . The model calculations indicate that in  $\text{CsI:Tl}$  (0.06 mole%) at room temperature, STE formation amounts to  $\leq 10\%$  of all electron hole pairs created in a 662 keV electron track. It shows furthermore that the fraction of all initial excitations in the track that eventually result in STE capture at  $\text{Tl}^+$  to form excited  $\text{Tl}^{+*}$  is  $\leq 5\%$ . This model result supports extension to  $\text{CsI:Tl}$  of the conclusion of Dietrich et al [22] noted above, namely that about 95% of energy transfer to  $\text{Tl}$  is by binary electron and hole transfer, with STE transfer (reaction #4) only a small contributor at perhaps 5%.

In summary, the detailed model results to be presented below show that the two main factors favoring binary electron-hole energy transfer over STE transfer in  $\text{Tl}$ -doped alkali halides are the rapid spatial separation of hot electrons from self-trapped holes [24], combined with the very large capture rate of conduction electrons on  $\text{Tl}^+$ . [14, 25] The capture rate of electrons on  $\text{Tl}^+$  (0.08%) was shown by picosecond absorption spectroscopy [25] to be even larger than the capture rate of electrons on self-trapped holes so that doping  $\text{CsI}$  with  $\sim 0.08$  mole%  $\text{Tl}$  ( $\approx 0.3$  wt% in melt) strongly inhibits STE formation. As a result of these findings, we will not consider reaction #4 involving STE energy transfer when seeking an explanation of the main 3 scintillation decay times in  $\text{CsI:Tl}$ .

A particular puzzle that we seek to answer in the rest of this section can be phrased as follows: Experiments have revealed three distinct decay components in  $\text{CsI:Tl}$  of 730 ns, 3.1  $\mu\text{s}$ , and 16  $\mu\text{s}$ , but apparently only the reactions #2 and #3 are available to account for them. Therefore it seems that at least one of the two main reactions (#2 or #3) must be contributing two distinct decay components of the scintillation pulse. How can that be? We look to plots of the time-dependent radial population and reaction rate from the model for insight.

## B. Time-dependent radial population and reaction rate plots

A good way to visualize the progress of various parts of the recombination process in the modeled track is to plot populations or reaction rates as a function of radius at a sequence of times for a given on-axis excitation density. Figure 6(a,b) plots the initial hole distribution along with  $\text{Tl}$ -trapped electron distributions ( $\text{Tl}^0$ ) in the critical first 10 picoseconds when hot-electron diffusion drives radial dispersal of electrons [24, 37] that are trapped in picoseconds as  $\text{Tl}^0$  (measured rate constant  $3 \times 10^{11} \text{ s}^{-1}$  for nominally 0.08 mole%  $\text{Tl}$  [14, 25]). This freezes in a charge-separated starting distribution of trapped electrons at larger radii of 40 nm or more and self-trapped holes close to the core in a radius of about 3 nm. As mentioned above, this electron-hole separation together with electron trapping as  $\text{Tl}^0$  discourages self-trapped exciton formation and is probably the main reason for the finding by Dietrich, et al [22] cited earlier that energy transport in  $\text{Tl}$ -activated  $\text{KI}$  and  $\text{NaI}$  occurs dominantly by binary electron and hole transport rather than STE transport. On longer time scales, as we shall see below, the  $\text{STH}$  will diffuse outward and ultimately electrons thermally released from  $\text{Tl}^0$  will diffuse inward. In both cases, the carrier diffusion is assisted by the strong internal electric field set up by the early charge separation seen in Fig. 6 particularly at high excitation density.

In Fig. 6(a), the population concentration is multiplied by the radius to produce a result proportional to the number of carriers present at each radius. Due to hot-electron dispersal, the number of trapped electrons peaks at about 25 nm when thermalization and electron trapping on the  $\text{Tl}$  activator have ended. As described in Ref. [14], we set the hot-electron diffusion coefficient of the undoped  $\text{CsI}$  host in our model to reproduce the same radial distribution of electrons thermalized after 4 ps in  $\text{CsI}$  as calculated by Wang et al [24], a mean radius of about 50 nm with some electrons dispersed as far as 200 nm. Upon including 0.08 mole%  $\text{Tl}$  in the modeled  $\text{CsI}$  with its measured electron capture rate constant of about  $3 \times 10^{11} \text{ s}^{-1}$  Ref.[25], the 25-nm mean radius of  $\text{Tl}^0$  population in Fig. 6(a) is found. Appreciable numbers of trapped electrons extend as far as 100 nm and beyond. The radially weighted plotting format of Fig. 6(a) was used in Ref. [14] with mixed units of  $\text{nm}/\text{cm}^3$ , chosen so that division by the radius in nm recovers the local population density at that radius in  $\text{cm}^{-3}$ . Figure 6(b) simply plots the carrier concentrations vs. radius. The reaction rates depend directly on the concentrations. We will use both plotting formats as appropriate in the analysis and discussions that follow. The narrow peaks at small radius in both frames of Fig. 6 are labeled as the initial hole population but equally well represent the electron population at  $t=0$ . Their values are divided by the factors 10 and 20 in (a) and (b) respectively to bring them on scale.

An immediate and striking conclusion to be drawn

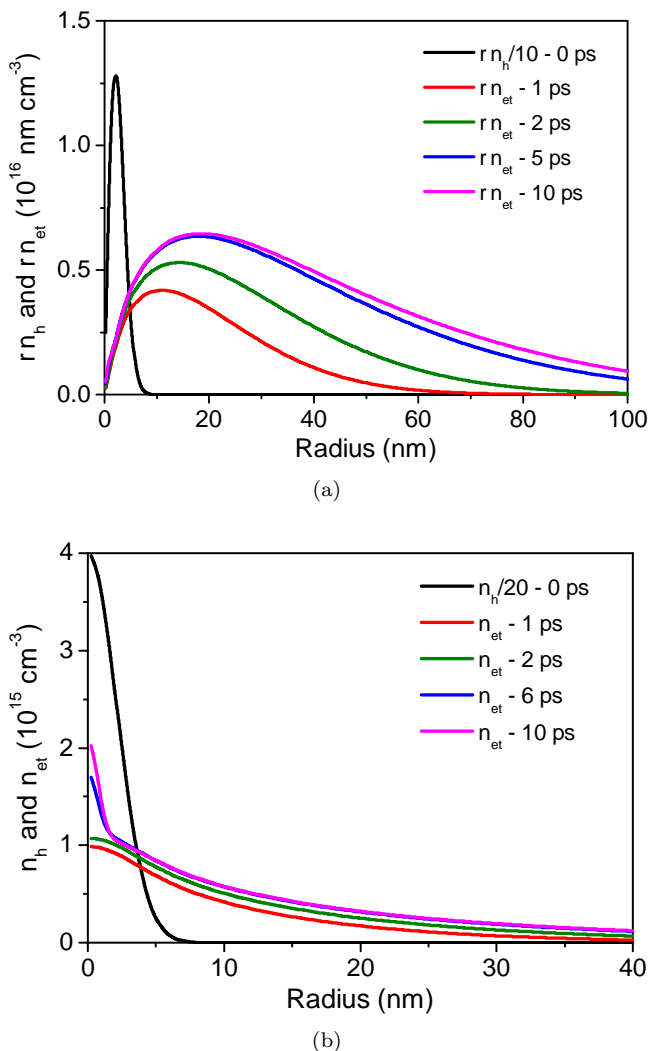


FIG. 6. The initial hole concentration profile,  $[\text{STH}] = n_h$ , is plotted together with the thallium-trapped electron concentration,  $[\text{Tl}^0] = n_{et}$ , at early times up to completion of electron trapping on Tl shortly after 5 ps. The on-axis excitation density is  $10^{20} \text{ cm}^{-3}$ . Two formats are presented. In frame (a), the population concentrations are multiplied by the radius to convey number of carriers vs. radius. In frame (b) the concentrations are reported directly.

from Fig. 6(a) is that the great majority of electrons are trapped within a few picoseconds on the Tl activator ions in CsI:Tl at radial locations that have little overlap with the self-trapped holes. The overlapped STH and  $\text{Tl}^0$  populations inside a radius of about 6 nm are immediately subject to recombination producing  $\text{Tl}^{+*}$  excited activators at a rate given by the term  $B_{et} n_{et} (1 - f_e) n_h$  in Eq. (6). Following the terminology introduced in earlier studies [20, 22, 23, 35], we have called this Reaction #2. In the finite-element solution of our rate model, the local rate of R#2 will be non-zero only when there are overlapping populations of  $\text{Tl}^0$  (local concentration  $n_{et}$ ) and STH (concentration  $n_h$ ) in the same cell. Thus the significant portion of  $\text{Tl}^0$  trapped electrons that do

not spatially overlap the STH distribution in Fig. 6(a) cannot immediately contribute to the Reaction #2 rate term. They become eligible if diffusion brings them into overlap. Such diffusion is assisted by the internal electric field set up between the separated trapped charges.

To illustrate, Fig. 7 plots the time dependent radial distributions of reaction #2 itself. The rate term that is responsible for reaction #2 is  $B_{et} n_{et} (1 - f_e) n_h \approx B_{et} n_{et} n_h$ , where  $n_{et}$  is the local density of  $\text{Tl}^0$  (electrons trapped on  $\text{Tl}^+$  activator),  $n_h$  is the local density of self-trapped holes (STH), and  $B_{et}$  is the bimolecular rate constant for this recombination of electrons and holes. The displayed results were calculated for an initial excitation density of  $10^{20} \text{ eh/cm}^3$  on-axis of the track.

Fig. 7(a) shows that for roughly the first 200 ps, the reaction #2 occurs only within a radius of about 6 nm where the STH and some of the  $\text{Tl}^0$  overlap from the beginning. Starting around 1 nanosecond, outward movement of the reaction zone tracking the diffusion of STH to overlap additional  $\text{Tl}^0$  at longer radius can first be seen. The occurrence of significantly slower STH diffusion rates evaluated at lower excitation densities of  $10^{19}$  and  $10^{18} \text{ eh/cm}^3$  (not plotted) demonstrates that Coulomb repulsion of the positive self-trapped holes in the track core significantly assists the STH transport outward. From about 4 ns onward, the outwardly advancing reaction zone leaves no significant activity in its wake because the  $\text{Tl}^0$  population (at density  $n_{et}$ ) is fully depleted by reaction with the dense advancing front of STH present at this excitation density and time range. Integrating the curve radially, we obtain the total R#2 rate at each considered time. The quantity  $n_{et} n_h$  proportional to the rate of R#2 is plotted in Fig. 8 on a semi-log scale. This is not a light decay curve, but a plot proportional to the reaction #2 rate for creating  $\text{Tl}^{+*}$  excited states for an initial excitation density of  $10^{20} \text{ cm}^{-3}$  on axis of the track. The  $1/e$  time for decay of the main R#2 rate is about 110 ns, corresponding to the straight line overlaid. Reaction #2 is itself a bimolecular recombination process. If the bimolecular rate term were the controlling factor in the decay at times longer than about 50 ns, we should expect a  $t^{-1}$  decay at long time rather than the exponential decay evident in Fig. 8. We regard the finding of first-order exponential decay kinetics for this reaction at long time as partial evidence of transport-limited reaction of spatially separated populations at longer times.

The curve in Fig. 8 begins with a fast spike of about 1 ns duration. Considering the initial stationary reaction zone seen in Fig. 7, we conclude that the fast spike represents reaction #2 in the initially overlapping STH and  $\text{Tl}^0$  populations, while the 110 ns decay component of the main part of the reaction #2 represents the transport-limited reaction rate of STH moving to encounter new  $\text{Tl}^0$  population. At the end of Fig. 7, reaction #2 can be seen taking place out to 80 nm, far beyond the initial zone of creation of STH, so STH diffusion out into the surrounding field of less mobile  $\text{Tl}^0$  has obviously been important. The  $\sim 1$  ns decay time of the spike of reac-

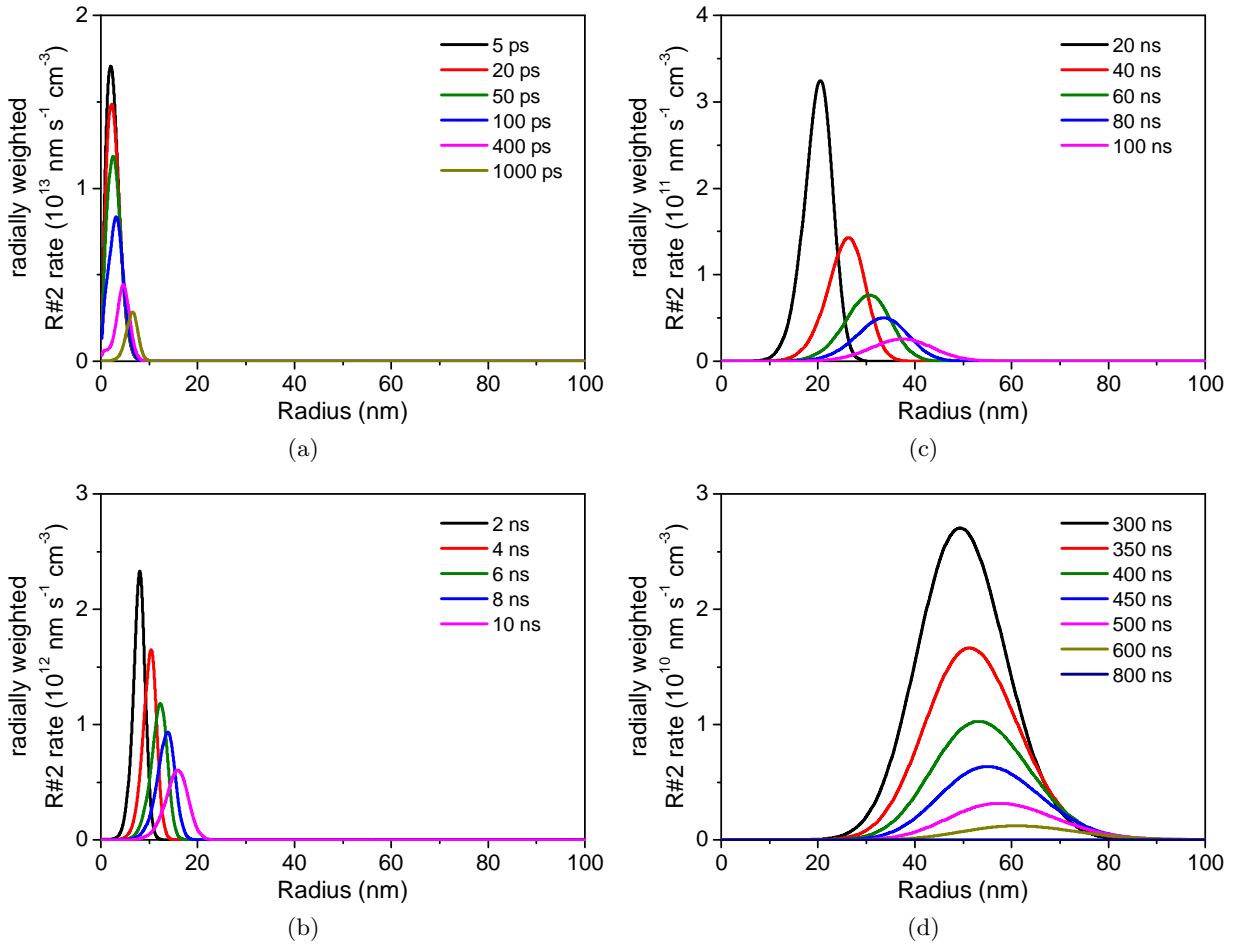


FIG. 7. The local rate of reaction #2 versus radius is plotted at evaluation times shown in the left two frames from 5 ps up to 10 ns and continuing in the right two frames from 20 ns to 800 ns. Reaction #2 ceases by 800 ns when the supply of STH has been consumed by this reaction and by the competing process of STH capture on  $\text{Tl}^+$  activator sites to create  $\text{Tl}^{++}$ .

tions consuming the initial overlapped populations and the 110 ns decay of the STH transport-limited reaction rate are two different manifestations of a single reaction which we and previous writers have termed Reaction #2 between STH and  $\text{Tl}^0$ .

Both the 1 ns and the 110 ns decays for reaction #2 to form  $\text{Tl}^{+*}$  excited states are faster than the photoluminescence decay time of the excited  $\text{Tl}^{+*}$  state itself (575 ns), so the two components do not lead to observably different decay times of light emission, but rather contribute different rise-time components to the so-called fast scintillation component decaying with an approximate 730 ns time constant. The full model calculation already demonstrated in Fig. 2 that the formation rate of  $\text{Tl}^{+*}$  excited states with a time constant of about 110 ns together with the 575 ns photoluminescence decay time of  $\text{Tl}^{+*}$  gives a good match to the observed 730 ns decay time of scintillation light. The prevailing view that reaction #2 is the main contributor to the 730 ns component is confirmed in this model, although we shall see later that Reaction #3 also contributes a decay component on the order of 800 ns. The model results in Figs. 7-9 furthermore con-

firm that reaction #2 expires too early (because of STH depletion) to be a contributor to either the 3  $\mu\text{s}$  or the 16  $\mu\text{s}$  scintillation decay components at the excitation density of  $10^{20}$  eh/cm<sup>3</sup> on-axis that is illustrated here.

Figure 9 below shows the radial population distributions of STH ( $n_h$ ),  $\text{Tl}^0$  ( $n_{et}$ ),  $\text{Tl}^{++}$  ( $n_{ht}$ ), and excited  $\text{Tl}^{+*}$  ( $n_t$ ), at six successive times from 10 ns to 10  $\mu\text{s}$ . The first population to take note of is STH. It can be seen on the radial axis that the STH population diffuses outward noticeably at times longer than about 10 ns. On the vertical axis, the number of STH can be seen decreasing rapidly with time in this early range as they encounter and combine with  $\text{Tl}^0$  to produce  $\text{Tl}^{+*}$  excited states (reaction #2) and with  $\text{Tl}^+$  to produce  $\text{Tl}^{++}$  trapped holes (setting up reaction #3). At 800 ns, virtually all STH have been consumed mainly by these two channels (i.e.  $n_h$  is written to zero when below 0.1% of its initial value shortly after 700 ns). At that point, R#2 has effectively stopped.

As seen in the 500 ns frame of Fig. 9, most of the STH are exhausted by this time but a population of  $\text{Tl}^{+*}$  excited activators ( $N_t$ ) produced by R#2 remain and are

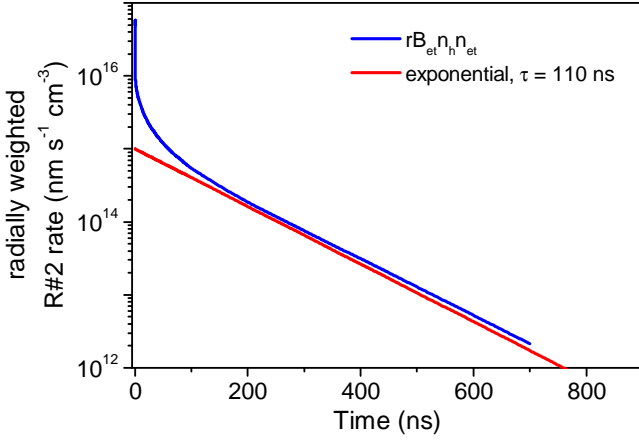


FIG. 8. Semi-logarithmic plot of spatially integrated rate of reaction #2 versus time, for on-axis excitation density of  $10^{20}$   $\text{eh}/\text{cm}^3$ .

available for continued radiative decay. In addition, the partly overlapped, partly separated distributions of  $\text{Tl}^{++}$  and  $\text{Tl}^0$  that will produce subsequent additions to  $\text{Tl}^{++}$  are evident. The overlapped  $\text{Tl}^{++}$  and  $\text{Tl}^0$  are immediately subject to recombination producing  $\text{Tl}^{++}$  at a rate given by the term  $B_{tt}n_{et}f_e n_{ht}$  in Eq. (6), which we have termed Reaction #3. The significant portion of  $\text{Tl}^0$  trapped electrons that are not spatially overlapping the  $\text{Tl}^{++}$  distribution in Fig. 9 cannot immediately contribute to this rate term for R#3, but become eligible if diffusion of electrons released from  $\text{Tl}^0$  and recaptured elsewhere as another  $\text{Tl}^0$  (assisted by the internal electric field of the separated charges that are clearly seen in Figs. 6 and 9) brings them into overlap. We have paraphrased the preceding two sentences from the discussion of R#2 illustrated in Fig. 7 earlier, because the phenomena relating to reaction-rate-limited and transport-limited components apply in very analogous ways to both R#2 and R#3. In the case of R#3, the rate-limited and transport-limited rates of creating excited  $\text{Tl}^{++}$  are both slower than the  $\text{Tl}^{++}$  radiative decay time, so it can be expected that both reaction rates of R#3 may be observed as separate decay components of light emission.

Note that particularly in the  $0.5 \mu\text{s}$  and  $1 \mu\text{s}$  frames of Fig. 9, the  $\text{Tl}^{++}$  trapped hole distribution develops a tail on its large-radius side extending unusually far into the  $\text{Tl}^0$  trapped electron population. In fact the  $\text{Tl}^{++}$  tail extends all the way to the peak of the  $\text{Tl}^0$  radial population distribution at about 65 nm. In the  $5 \mu\text{s}$  and  $10 \mu\text{s}$  frames of Fig. 9, the extended tail of  $\text{Tl}^{++}$  has disappeared. This behavior suggests qualitatively that in the time leading up to roughly  $0.5 \mu\text{s}$ , STH diffusion and capture on  $\text{Tl}^+$  created  $\text{Tl}^{++}$  overlapping  $\text{Tl}^0$  at a faster rate than Reaction #3 could consume them. This resulted in storage of spatially overlapped reactant populations. The tail of  $\text{Tl}^{++}$  population extending into the region of high  $\text{Tl}^0$  population seems to be one manifestation of that. After about  $0.8 \mu\text{s}$  when STH are effectively exhausted,

the overlapped populations of  $\text{Tl}^{++}$  and  $\text{Tl}^0$  should be the first consumed by R#3 in the few-microsecond time range. We suggest that this accounts for the  $3 \mu\text{s}$  decay component of R#3. When the main part of the stored-up overlapped reactant population is exhausted, as we might judge from disappearance of the  $\text{Tl}^{++}$  tail in the  $5 \mu\text{s}$  frame, subsequent decay of R#3 is governed by the transport of released and recaptured  $\text{Tl}^0$  electrons from their main population at large radius toward the reservoir of  $\text{Tl}^{++}$  at small radius. This transport-limited portion of R#3 is suggested to be responsible for the  $16 \mu\text{s}$  decay component. R#3 is itself bimolecular, and yet the  $16 \mu\text{s}$  decay component is found experimentally (and in this model calculation as well) to be approximately exponential, signifying first-order kinetics. This is consistent with its being a transport-limited reaction between spatially-separated reactants. Notice the parallel reasoning between this discussion of the origin of  $3 \mu\text{s}$  and  $16 \mu\text{s}$  decay components of R#3 and the origin of the 1 ns and 100 ns rise components of R#2. The difference is that R#3 is slower than the 575 ns photoluminescence decay time of excited  $\text{Tl}^{++}$ , while R#2 is faster than that radiative time.

Recall that we ruled out reaction #4 (STE energy transport) as the source of any of the three main decay components because of the implications of extreme charge separation and electron trapping in Fig. 6. By elimination of the alternatives, attention is now focused on reaction #3 to understand from additional model perspectives how both the medium and tail decay components can arise from it.

Figure 10(a-d) plots the radial dependence of the concentration of  $\text{Tl}^{++}$  excited states resulting from all reactions calculated for on-axis excitation density of  $10^{20}$   $\text{cm}^{-3}$ , sampled at times from 5 ps to  $10 \mu\text{s}$  as labeled in the legends. The time sequence increases going down the left column and then going down the right column, ending at  $20 \mu\text{s}$ . Notice that the radial scale range and the vertical axis range both change as time goes on. For the first 100 ps, the  $\text{Tl}^{++}$  excited states are formed at increasing rate "in place" defined by the initial STH distribution overlapping some  $\text{Tl}^0$  formed near the axis. The total number of excited states (integrated azimuthally and radially) is small in this stage. At times longer than about 200 ps, a shoulder progressing out to larger radius indicates the onset of significant STH diffusion, resulting in overlap with additional  $\text{Tl}^0$  to sustain the reaction #2. This continues out to 800 ns in frame (c), at which time the supply of STH is exhausted as we saw previously in Figs. 7 and 9. By this time, an underlying contribution from reaction #3 has developed, so  $\text{Tl}^{++}$  formation is maintained going forward beyond 800 ns.

These plots of  $\text{Tl}^{++}$  at various times give additional clues to the origin of the two distinct decay times found in the range longer than 730 ns, where Reaction #3 is the only substantial recombination reaction still taking place. Indeed, the last frame in Fig. 10 showing times from  $1.5 \mu\text{s}$  to  $20 \mu\text{s}$  displays a distinct change in height,

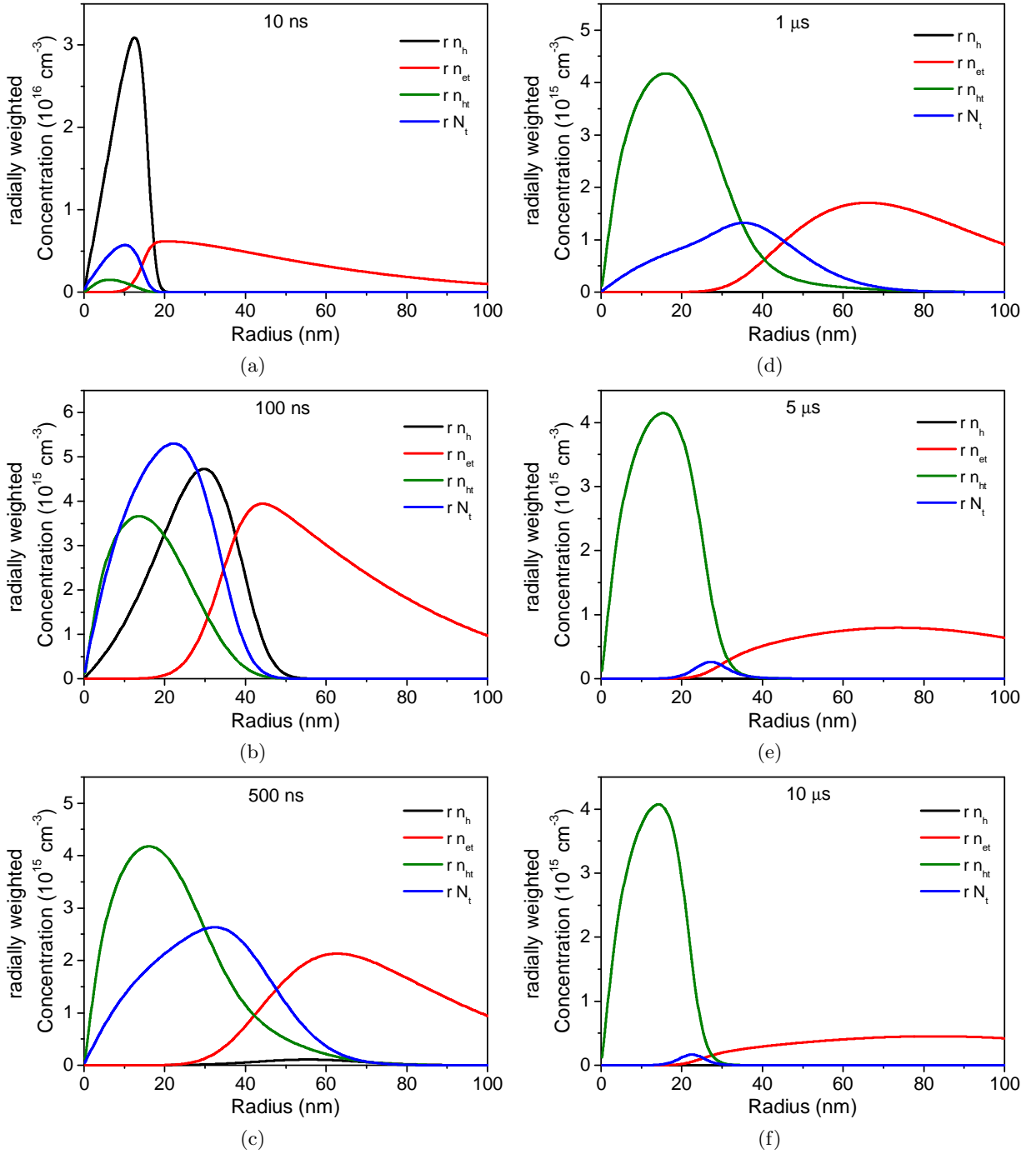


FIG. 9. Plots proportional to azimuthally integrated local density of STH ( $r n_h$ ),  $Tl^0$  trapped electrons ( $r n_{et}$ ),  $Tl^{++}$  trapped holes ( $r n_{ht}$ ), and  $Tl^{++}$  trapped excitons  $r N_t$  are displayed as a function of radius at six indicated times between 10 ns and 10  $\mu s$ . The plots correspond to on-axis excitation density of  $10^{20}$  eh/cm<sup>3</sup>.

width, and shift of radial position versus time for the peak in Tl-trapped exciton population, starting after 3  $\mu s$ .

The dominant radial distribution for times from 1.5 to 3  $\mu s$  is a peak in  $Tl^{++}$  fixed at about 36 nm, overlying a background that slopes downward with increasing radius. The background falls away due to  $Tl^{++}$  radiative decay

over the interval from 0.8 to 1.5  $\mu s$ , revealing the stationary peak at 36 nm quite clearly as a main contributor to the rate of Tl excited state production during this few-microsecond range. Considering the 575 ns decay time of  $Tl^{++}$ , the time interval of dominance of this 36-nm peak in radial distribution of reaction #3 production of  $Tl^{++}$  lines up with the experimental 3  $\mu s$  decay compo-

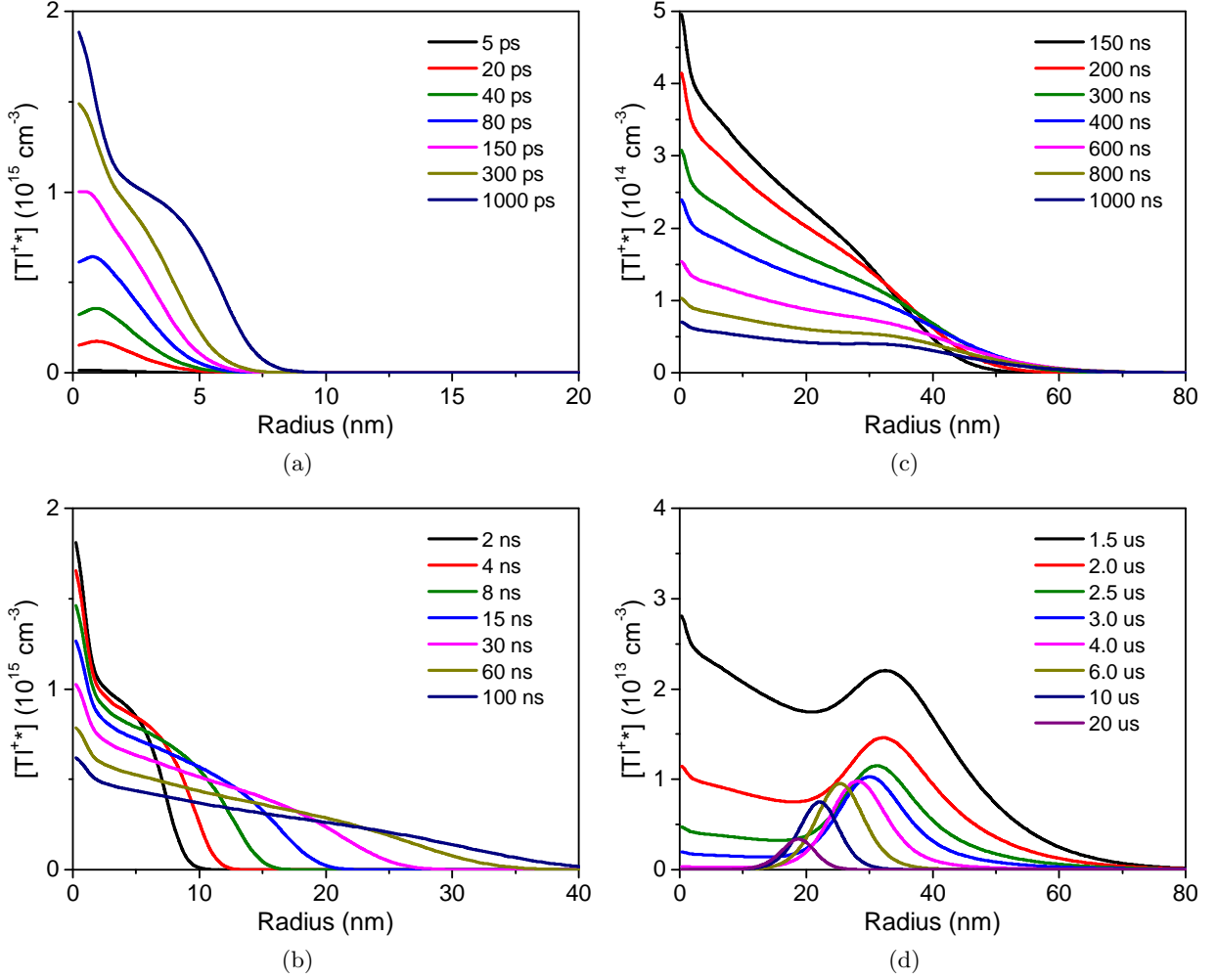


FIG. 10. The  $Tl^{+*}$  excited state ( $N_t$ ) concentration distribution resulting from all reactions at on-axis excitation density of  $10^{20} \text{ cm}^{-3}$  is plotted versus radius at times sampled from 5 ps to 20  $\mu\text{s}$ . Notice that the radial scale range and the vertical axis range both change as time goes on.

ment of light emission. Recall that in Fig. 9 we could see a tail of the  $Tl^{++}$  distribution penetrating deep into the  $Tl^0$  population during the few-microsecond period, suggesting that overlapped reactants were being stored in the radial range from 30 to 60 nm during the first 0.5  $\mu\text{s}$ , and that afterward they were being consumed by R#3. We may conclude that the peak of the radial reaction zone producing  $Tl^{+*}$  in Fig. 10 from roughly 1 to 3  $\mu\text{s}$  remains stationary because it is running mainly on the overlapped populations that were stored previously. When those stored overlapped populations are exhausted, the R#3 reaction zone begins to shift inward toward small radius, as the continued R#3 depends on diffusion of electrons untrapped from  $Tl^0$  to find  $Tl^{++}$  at smaller radius.

Starting at about 3  $\mu\text{s}$  in Fig. 10(d), the formerly stationary radial peak in  $Tl^{+*}$  population shifts toward smaller radius as just noted. It assumes a smaller width and gradually decreasing height out to 20  $\mu\text{s}$ . Empiri-

cally, it seems natural to associate this radially shifting and slowly decreasing zone of R#3 with the 16  $\mu\text{s}$  decay component. This strongly suggests that the 3  $\mu\text{s}$  and 16  $\mu\text{s}$  decay components both come from R#3 (thermally ionized  $Tl^0$  electrons reacting with stored  $Tl^{++}$  trapped holes), with the distinct decay times rooted in different spatial distributions of the reactants, calling into temporary dominance different rate terms in Eqs. (4-6).

When the transport arrival rate of carriers increases the product of reactants faster than the bimolecular reaction rate governed by  $B_{tt}^0 n_{ht} n_{et} f_e$  can decrease it, the R#3 rate producing  $Tl^{+*}$  is not transport limited. Also if the product of local reactant densities built up from previous trapping added to the transport into that location supports a bimolecular recombination rate faster than the arrival of new overlapped populations, once again the R#3 rate producing  $Tl^{+*}$  is not transport limited. The rate in these cases will be set by the bimolecular rate constant  $B_{tt}^0$  multiplying the local product of den-



sities "in place". As time goes on, the bimolecular rate of "in place" reactions will consume the stored excess population of overlapped carriers. We propose that such reaction "in place" combined with radiative decay is happening in Fig. 10(d) between about 1.5 and 3  $\mu\text{s}$ . The bimolecular rate falls until it equals the rate of increase of the reactant density product due to transport processes (1) and (2) listed above. When the reaction rate becomes equal to the transport rate, the rate of the bimolecular reaction is transport limited, and should be determined partly by the concentration gradient and electric field that drive directional transport. In contrast, the rate term  $B_{tt}^0 n_{ht} n_{et} f_e$  for bimolecular recombination does not depend directly on concentration gradients or electric fields. In this way, two distinct decay components of the R#3 can arise.

Figure 2 showing calculated light emission as a function of time confirms that the rates of  $\text{Ti}^{+*}$  production which are dissected in Fig. 10 do indeed produce scintillation decay times corresponding to the observed values of 730 ns, 3.1  $\mu\text{s}$ , and 16  $\mu\text{s}$ . We conclude again that the latter two are due, respectively, to non-transport-limited and to transport-limited bimolecular reaction #3 between  $\text{Ti}^{++}$  and  $\text{Ti}^0$ .

Figures 11-13 below provide further support for this conclusion. Figure 11 illustrates the transition from "in-place" consumption of local stored densities of reactants to transport-limited reaction at a slower rate. The radially weighted rate of change of local density of  $\text{Ti}^0$  due only to transport is plotted in the solid curves, while the radially weighted rate of change of local density of  $\text{Ti}^{++}$  at corresponding times is plotted in the dashed curves. The latter are fully negative because production of any new  $\text{Ti}^{++}$  ceased shortly after 700 ns, the first curve shown in this figure.  $\text{Ti}^{++}$  are assumed not to diffuse on time scales of interest in scintillation, so the reason for their population to decrease in this model is R#3, in which a  $\text{Ti}^{++}$  and a  $\text{Ti}^0$  are annihilated as a pair with production of  $\text{Ti}^{+*}$ . Thus the dashed curves also represent identical loss of  $\text{Ti}^0$  by R#3 recombination. In these terms, Fig. 11 may be considered to compare radially weighted profiles of rate of change of  $[\text{Ti}^0]$  due to reaction #3 occurring "in place" (Recombination, dashed curves) and due only to transport by diffusion and electric current (Transport, solid curves) at the indicated times.

When the transport-limited regime is attained, every  $\text{Ti}^0$  arriving in the reaction zone by diffusion and electric current transport of the thermally released electron should correspond pairwise with the loss of a  $\text{Ti}^{++}$  from the reaction zone. The positive peak of the  $\text{Ti}^0$  transport curve should come to have the same height, width, and radial position as the inverted peak of the  $\text{Ti}^0$  and  $\text{Ti}^{++}$  pairwise consumption curve. It can be seen in Fig. 11 that this occurs for times of approximately 3  $\mu\text{s}$  and greater. At earlier times, the dashed curve exceeds the transport peak of  $\text{Ti}^0$  arrivals in height and width, consistent with the consumption of locally stored  $\text{Ti}^{++}$  and

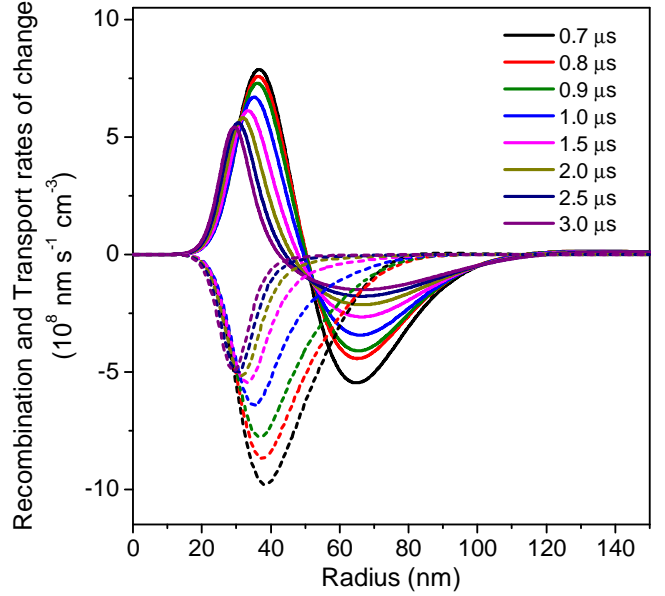


FIG. 11. Radially weighted profiles of rate of change of  $[\text{Ti}^0]$  due to reaction #3 occurring "in place" (Recombination, dashed curves) and due only to transport by diffusion and electric current (Transport, solid curves) are compared at the indicated times. After about 3  $\mu\text{s}$ , the rate of loss of  $[\text{Ti}^0]$  (and identically of  $[\text{Ti}^{++}]$ ) approaches equality with the positive gain of  $[\text{Ti}^0]$  due to transport, indicating onset of the transport-limited regime.

$\text{Ti}^0$  populations to feed part of the bimolecular recombination via reaction #3 during the 1-3  $\mu\text{s}$  interval of the middle decay component.

Figure 12 presents a time sequence from 100 ps through 30  $\mu\text{s}$  for the R#3 rate term  $B_{tt}^0 n_{ht} n_{et} f_e$ , where  $n_{ht}$  is the  $\text{Ti}^{++}$  density,  $n_{et} f_e$  is the local density of  $\text{Ti}^0$  that are thermally ionized in equilibrium, and  $B_{tt}^0$  is the bimolecular rate constant for reaction #3.

Figure 12 confirms much of what was seen in earlier radial representations of different data, particularly Fig. 10. The rate of R#3 increases rapidly at small radius over the first 1000 ps. In the overview of the earlier times in Fig. 12(a), we can see that the reaction rate for R#3 initially grows versus time, inside 10 nm radius, for about the first 1000 ps. Since the density profile for  $\text{Ti}^0$ -trapped electrons,  $n_{et}$ , was established in the first 10 ps, the growth in height of this  $B_{tt}^0 n_{ht} n_{et} f_e$  reaction peak is due to increase of  $n_{ht}$ , the density of  $\text{Ti}^{++}$ , by capture of STH from the intense peak at small radius seen in Fig. 6(a). This is governed by the rate term  $S_{1h} n_h$  appearing in Eq. (2) as a loss and in Eq. (5) as a source term. The evolution from about 10 ns to 0.5  $\mu\text{s}$  is mainly that of a radially translating reaction zone tracking the STH diffusion front as it creates new  $\text{Ti}^{++}$  overlapping existing  $\text{Ti}^0$ .

From 0.5  $\mu\text{s}$  to about 3  $\mu\text{s}$ , the width of the zone decreases rapidly as its peak shifts inward toward smaller radius. This coincides in time with the evidence we have

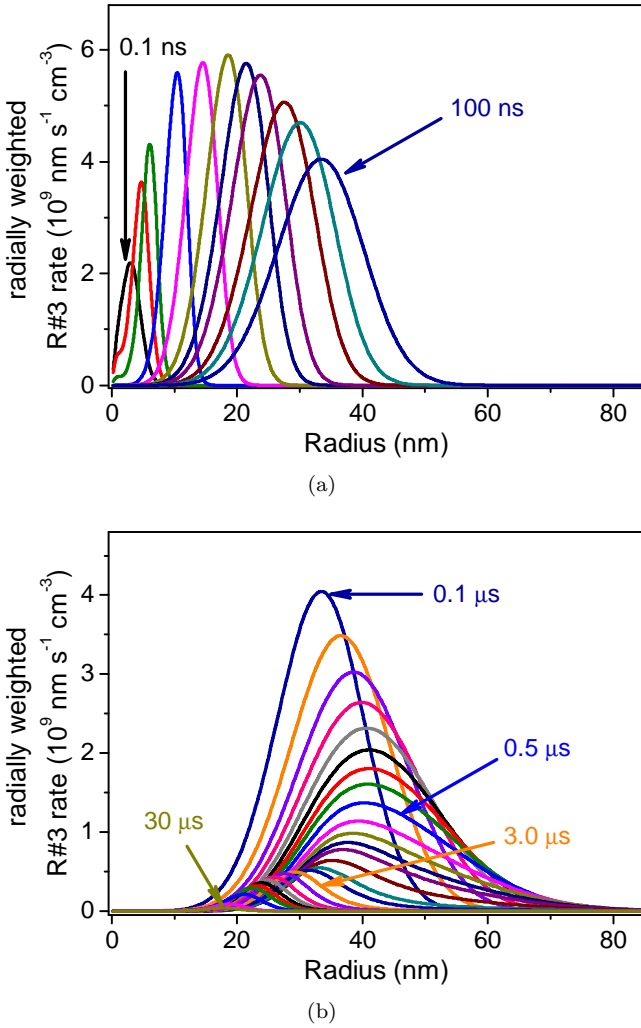


FIG. 12. Radially weighted profiles of R#3 reaction rate are plotted for times (a) 0.1 ns, 0.5, 1, 5, 10, 20, 30, 40, 60, 80, 100 ns, and (b) 0.1  $\mu\text{s}$ , 0.15, 0.2, 0.25, 0.3, 0.35, 0.4, 0.45, 0.5, 0.6, 0.7, 0.8, 0.9, 1, 1.5, 2, 3, 4, 5, 6, 7, 8, 9, 10, 20, 30  $\mu\text{s}$ . The radial weighting factor  $r$  comes from azimuthal integration of the cylindrical track to assess the total reaction rate versus radius. Mixed units of  $10^9 \text{ nm s}^{-1} \text{ cm}^{-3}$  are used as in Ref. [14] so that division by the radius in nm recovers the local reaction rate at that radius in units of  $\text{s}^{-1} \text{ cm}^{-3}$ .

noted earlier for consumption of stored overlapping  $\text{Tl}^{++}$  and  $\text{Tl}^0$  populations around 40 to 60 nm radius that were accumulated faster than the R#3 reaction could occur in the preceding 0.5  $\mu\text{s}$ . Thereafter until the last plot at 30  $\mu\text{s}$ , a narrow reaction zone moves inward as a transport-limited reaction fueled by arrival of  $\text{Tl}^0$  (diffusing by electron release and recapture) from the reservoir at larger radius. This is the same sequence that was evident in Fig. 10, told this time from the perspective of the R#3 rate term.

The profile of R#3 represented in Fig. 12 was integrated over the radial coordinate to obtain the total reaction #3 rate as a function of time. The resulting time dependence of the R#3 rate is plotted in Fig. 13(d) for

excitation density  $10^{20} \text{ eh/cm}^3$  on axis, the same value used for the illustrations in Figs. 6-12. In Fig. 13, we also show results for  $10^{17}$ ,  $10^{18}$ , and  $10^{19} \text{ eh/cm}^3$  on axis and in all the frames we have attempted to reconstruct the decay curve in terms of the three exponential decay times, 730 ns, 3.1  $\mu\text{s}$ , and 16  $\mu\text{s}$  found to fit the experimental scintillation decay data (662 keV) [12]. As shown earlier, reaction #2 ( $\text{STH} + \text{Tl}^0 \rightarrow \text{Tl}^{+*}$ ) is mainly responsible for the 730 ns scintillation decay, and that reaction is not represented in Fig. 13. Nevertheless, R#3 turns out to exhibit a fast component of the reaction rate decay in the range of 700 ns as well, so the 730 ns decay time was included in the analysis. The main interest driving this analysis was in the 3.1  $\mu\text{s}$  and 16  $\mu\text{s}$  components of R#3. We have seen that R#2 goes to completion within 800 ns at  $10^{20} \text{ eh/cm}^3$  and 1.4  $\mu\text{s}$  at  $10^{17} \text{ eh/cm}^3$ , so the two longer decay components of scintillation should arise mainly from R#3. Furthermore, since these longer decay times significantly exceed the 575 ns photoluminescence decay time of  $\text{Tl}^{+*}$ , the longer components of scintillation decay can be expected to track the decay of the total R#3 reaction rate producing  $\text{Tl}^{+*}$ .

The three-component analysis in Fig. 13 shows reasonably good fits at  $10^{17}$ ,  $10^{18}$  and  $10^{19} \text{ eh/cm}^3$  but a substantial under-representation at  $10^{20} \text{ eh/cm}^3$  from about 5  $\mu\text{s}$  to 30  $\mu\text{s}$ . This is a reminder that the scintillation is a weighted sum over many contributing local excitation densities. Furthermore, the analysis indicates a reduction of the 730 ns component as the excitation density is lowered, trending toward a mostly two-component sum of 3.1  $\mu\text{s}$  and 16  $\mu\text{s}$  decay for the R#3 curve at  $10^{17} \text{ eh/cm}^3$ .

The collective effect of all the excitation densities to R#3 can be calculated by weighting each according to its frequency of occurrence in a 662 keV electron deposition using GEANT4. This procedure is analogous to the method for weighting local light yield in our full scintillation model. The result for weighted R#3 is shown in Fig. 14. The model-calculated R#3 decay curve in blue is matched fairly well by the sum of 730 ns, 3.1  $\mu\text{s}$ , and 16  $\mu\text{s}$  components in orange. Two small discrepancies around 4  $\mu\text{s}$  and 16  $\mu\text{s}$  remain and are similar to the full model fits of scintillation decay in Fig. 2. If the 3.1  $\mu\text{s}$  decay time is replaced by a 4  $\mu\text{s}$  decay time, nearly exact matching of the calculated R#3 curve is obtained, but we will stay with the set of fixed decay times from the experimental study [12].

We regard Fig. 14 as confirmation that the R#3 reaction rate for the weighted sum of excitation densities in a 662 keV track can be well represented by the three decay time components of scintillation [12], even though that representation fails to some degree at high excitation density around  $10^{20} \text{ eh/cm}^3$ . Two notable features have emerged at  $10^{20} \text{ eh/cm}^3$  in Fig. 13(d). The 3.1  $\mu\text{s}$  component has yielded strength to a 730 ns component in the fitting at high density. Effectively, what was the faster (3  $\mu\text{s}$ ) of two main slow components of R#3 at lower excitation densities has become faster still at high

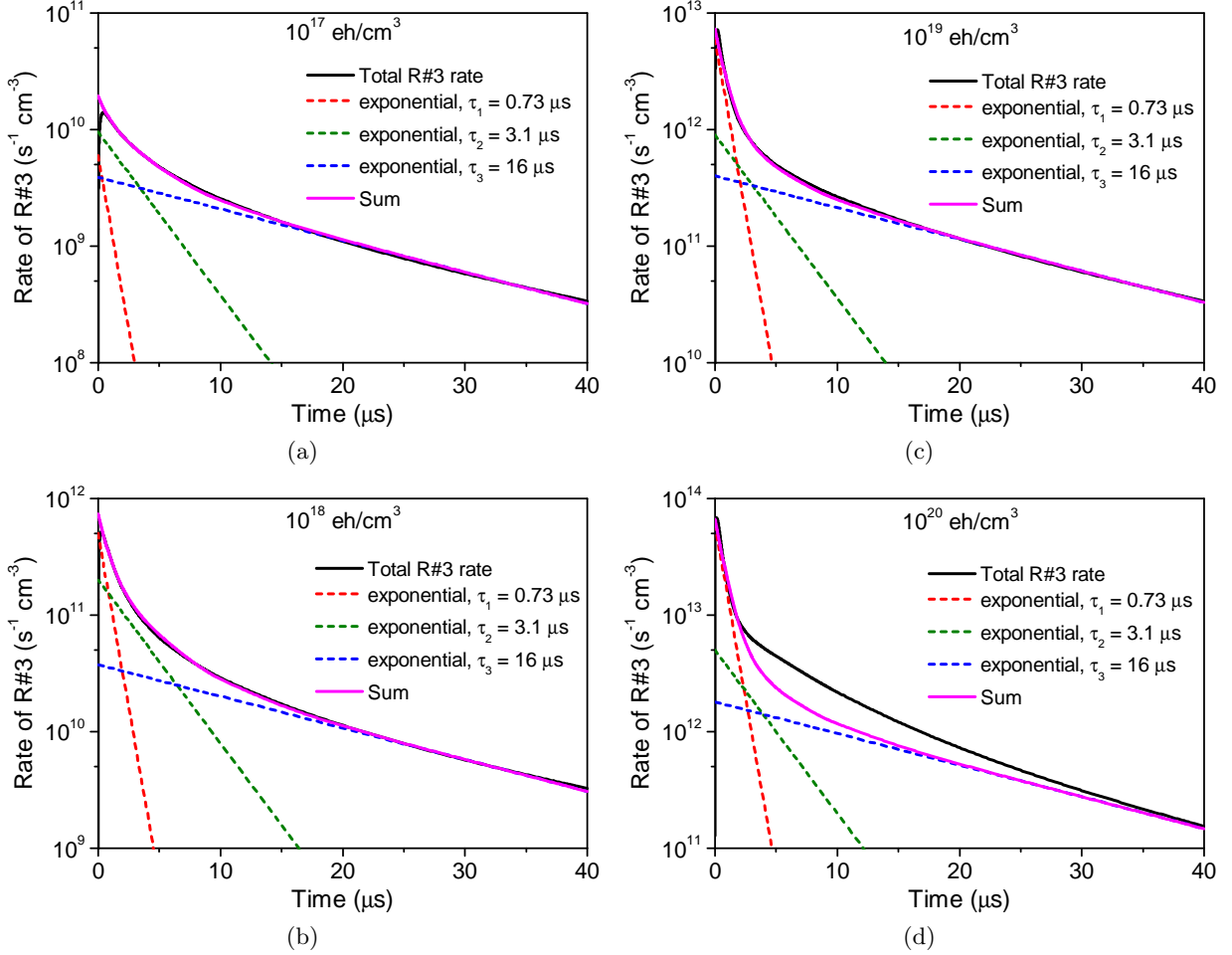


FIG. 13. The spatially integrated rate of reaction #3 (black curve) is plotted as a function of time on semi-log scale for excitation densities of (a)  $10^{17}$ , (b)  $10^{18}$ , (c)  $10^{19}$ , and (d)  $10^{20}$   $\text{eh}/\text{cm}^3$ . This model result represents the time-dependent rate of change of the number of  $\text{Tl}^{+*}$  excited activators due solely to R#3. It is the main contributor to the  $\text{Tl}^{+*}$  emitting state population at times longer than 700 ns. Three exponential decay components of 730 ns, 3.1  $\mu\text{s}$ , and 16  $\mu\text{s}$  found to characterize 662 keV scintillation decay [12] are fitted and displayed along with their sum in the magenta curve that can be compared to the model-calculated black curve.

density and will contribute light in the same general time range as the main 730 ns fast component of scintillation due to R#2. In experimental observations of scintillation pulse shape versus gamma energy, this will appear as an increase in the ratio of fast compared to slow and tail components at low gamma energy, i.e. high excitation density. This is the observed experimental trend. Part of the reason is identified with increasing contribution of R#3 in the same time range as the fast component of mainly R#2 light emission. Other reasons for this energy dependence of pulse shape can be found in the kinetics and spatial dependence of R#2 itself as already discussed.

In addition, Fig. 13 shows that the "tail" decay time trends to a shorter value than 16  $\mu\text{s}$  at the higher excitation densities, especially  $10^{20}$   $\text{eh}/\text{cm}^3$ . The experimental trend found in Ref. [12] was that at low gamma energy the tail decay time became slightly faster, e.g.  $14 \pm 3$   $\mu\text{s}$

at 6 keV.

Fig. 13 shows that the empirical "3  $\mu\text{s}$  decay time" is not a single identified process with that decay time, but is the weighted sum of multiple decay times dependent on excitation density that vary through the roughly 10  $\mu\text{s}$  to 0.7  $\mu\text{s}$  range as excitation density encountered in a track spans the corresponding densities. This leads us finally to reconsider whether the characterization of the scintillation decay by three exponential components need imply that the light is coming from rigorous "exponential decay processes", i.e. pure first-order decay. It does not. The fast and slow components are demonstrably not rigorous exponential functions. Although this model provided justification for why the transport-limited tail component would obey an approximately first-order decay law, exact first-order decay would not result given the complexity of the tracks, and the data themselves are frankly too noisy to assert exact exponential decay

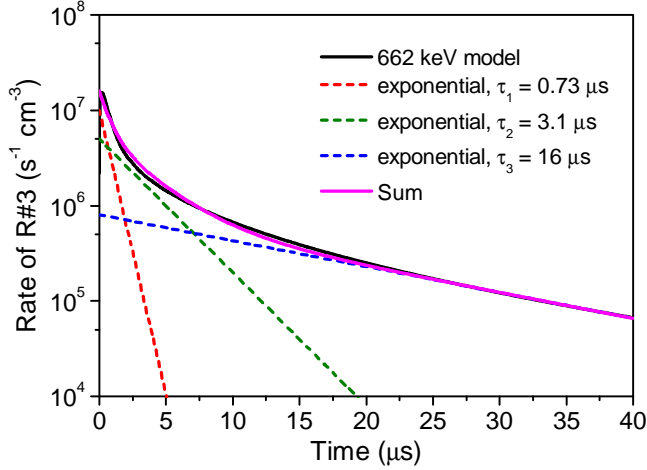


FIG. 14. The rate of reaction #3 as a function of excitation density was weighted by the probability of occurrence of each excitation density in a 662 keV electron track based on GEANT4 simulations and is displayed versus time in the blue curve. Three exponential decay components of 730 ns, 3.1  $\mu$ s, and 16  $\mu$ s found to characterize 662 keV scintillation decay [12] are fitted and displayed along with their sum in the magenta curve that can be compared to the model-calculated black curve.

in the tail. Whether multi-exponential or nonexponential with identified fast, slow, and tail components near 0.73, 3.1, and 16  $\mu$ s, these are the data modeled.

## VI. ORIGIN OF ANTICORRELATED FAST AND TAIL PROPORTIONALITY TRENDS AT ROOM TEMPERATURE

As could be seen in Fig. 5, the model predicts proportionality curves of the fast and tail components of scintillation showing the same remarkable anticorrelation of trends for these two components as was found in experiment [12]. The measured fast component falls as energy increases from 16 keV to 662 keV, while the tail component rises over the same increasing energy interval. To get at the physical mechanisms behind this anticorrelated behavior of fast and tail proportionality curves, we make use of the results in the previous section confirming that the fast decay component (730 ns) is mainly due to reaction #2, and the tail component (16  $\mu$ s) is due to the transport-limited part of reaction #3. As has been discussed, the rate term in Eq. (6) that is responsible for reaction #2 is  $B_{et}n_{et}(1 - f_e)n_h$ , and the rate term responsible for reaction #3 is  $B_{tt}^0n_{et}f_en_{ht}$ . These are not light outputs, but they both feed the  $Tl^{+*}$  population from which light is emitted.

In Fig. 15, the excitation density dependences of the yields of R#2 and R#3 producing  $Tl^{+*}$  excited states are plotted in blue and red, respectively. We could call this the "local yield of reactions #2 and #3" in analogy to what we have previously called local light yield as a

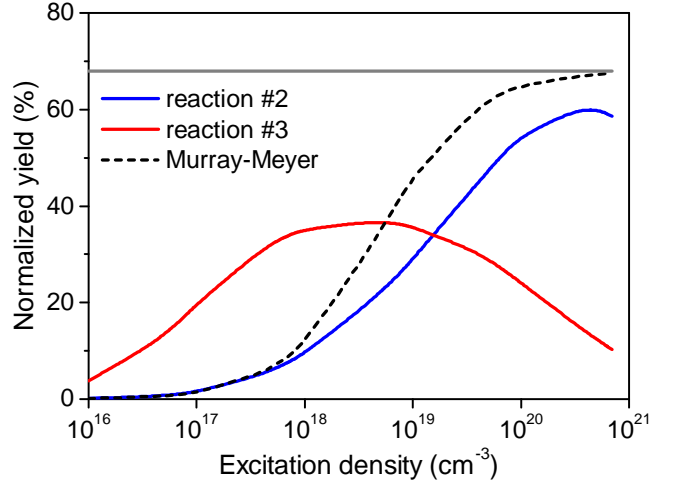


FIG. 15. The time- and space-integrated yields of the reactions #2 and #3 are plotted versus initial on-axis excitation density in the solid blue and red curves, respectively. The yield is integrated from zero to 40  $\mu$ s.

function of excitation density. The dashed black curve and grey horizontal line labeled "Murray-Meyer" will be discussed later.

Look first at the blue solid curve for the yield of reaction #2. It starts near zero at very low excitation density and rises with a concave upward curvature consistent with the fact that reaction #2 is bimolecular in populations whose initial values scale roughly with excitation density. We say "roughly" because it should be apparent from the above discussion and radial plots that the product of overlapping STH and  $Tl^0$  densities varies dramatically in time and space as a result of hot-electron diffusion in the beginning followed by electric-field driven diffusion re-uniting free carriers and trapped carriers over time. But in sweeping terms, the supply of reactant populations that can participate in transport and recombination is roughly proportional to the initial excitation density, so we should not be surprised that the R#2 yield (i.e. the blue curve) looks similar to the dashed curve (discussed below) which is a bimolecular yield competing with a linear loss in a limited population. Above about  $7 \times 10^{19}$  eh/cm<sup>3</sup>, the blue curve starts to bend over and eventually turns downward. That trend is understandable first because the supply of reacting carriers is limited, so it must be a saturating yield that finally bends toward a finite value if there are no losses. The limit of the saturating yield is lowered by 2<sup>nd</sup> order quenching and the sharp turn-down above  $4 \times 10^{20}$  eh/cm<sup>3</sup> can be attributed to 3<sup>rd</sup> order Auger quenching.

Bearing in mind that Fig. 15 plots local reaction yield as a function of excitation density, not light yield as a function of gamma energy, one nevertheless can see that the fast reaction #2 curve has a shape consistent with the proportionality curve of the fast 730 ns scintillation component shown in the experimental results of Fig. 5(a). In



making this comparison, we qualitatively associate high gamma energy with predominantly low excitation density and low gamma energy with predominantly high excitation density.

Now focus on the solid red curve plotting the local yield of the slower R#3. For excitation densities above  $10^{18}$  eh/cm<sup>3</sup> that comprise most of the energy deposition in high energy electron tracks, the curve of R#3 yield is flat or turns downward with increasing excitation density. This trend is anticorrelated with the increasing yield of R#2 versus excitation density, just as seen in the experimental fast and tail proportionality versus gamma energy (Fig. 5(a)). The essential reason for this anticorrelation is quite basic, namely the two processes compete for the same STH supply in two different kinetic orders. Reaction #2 ( $STH + Tl^0 \rightarrow Tl^{+*}$ ) is bimolecular in excitation products and therefore wins at high excitation density over the first-order process of  $Tl^{++}$  formation ( $STH + Tl^+ \rightarrow Tl^{++}$ ). The latter process obeys first-order kinetics because  $Tl^+$  is a crystal dopant, not an excitation product. Since  $Tl^{++}$  is a reactant for R#3, we see the result of the competition as a decrease in R#3 at high density in Fig. 15. The reaction #3 rate term is proportional to the product of two trapped carrier populations, both of which are essentially the "leftovers" after completion of the faster reaction #2. By about 3  $\mu$ s when we can first clearly identify the tail component, R#2 has run to completion and has consumed 54% of the starting STH and  $Tl^0$  at  $10^{20}$  eh/cm<sup>3</sup> versus 9.5% of the starting STH and  $Tl^0$  at  $10^{18}$  eh/cm<sup>3</sup>, according to the model results. Most of the STH not used in R#2 were converted by capture into  $Tl^{++}$  and will serve as one reactant for R#3. Most of the  $Tl^0$  not used in R#2 will be used as the other reactant in R#3. The yield of reaction #3 scales approximately as the product of two nearly equal populations that are both "leftovers" after completion of reaction #2. In those general terms, the yield of R#3 in this system must be anticorrelated with the yield of R#2 versus excitation density and therefore versus gamma or electron energy in the reversed sense of how particle energy and effective excitation density are approximately related. The anticorrelation displayed in the experimental measurements of Fig. 5(a) is a direct consequence. The ratio of carriers being used in R#2 or left over for R#3 is influenced by the electric field assisted transport of STH in the first phase, which is dependent on excitation density.

Reaction #3 is itself bimolecular since the  $Tl^{++}$  and  $Tl^0$  reactants (in the sense of the corresponding rate term in Eq. (6)) are both excitation products. This accounts for the rising slope of R#3 with excitation density at low densities in Fig. 15, i.e. before R#2 begins to deplete the STH supply in 2<sup>nd</sup> order faster than the 1<sup>st</sup>-order  $STH + Tl^+$  capture can use them. The fact that R#3 starts out larger than R#2 at low carrier densities is also understandable because a large fraction of STH are converted to  $Tl^{++}$  at low excitation density where first-order capture on numerous activators competes well

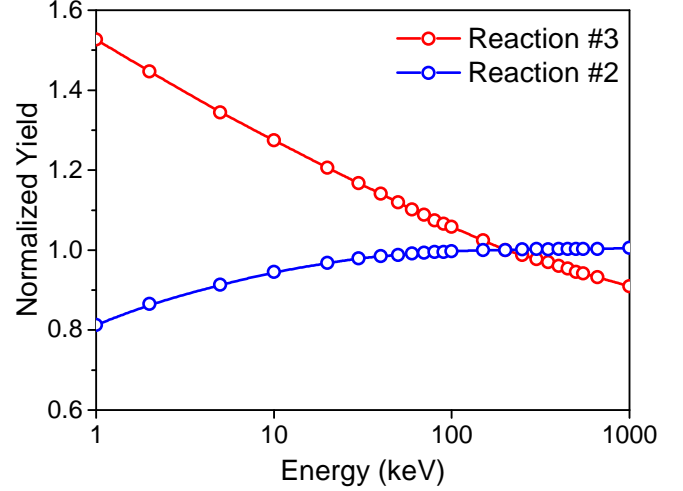


FIG. 16. The yields of reaction #2 and reaction #3 evaluated after 40  $\mu$ s are plotted versus initial electron energy.

with bimolecular recombination.

Proceeding from reaction yields versus excitation density to reaction yields versus electron energy, Fig. 16 plots the result of weighting the reaction yields at various densities in Fig. 15 by the probability of each density occurring in the Geant4 simulations for a given initial electron energy. Repeating for various electron energies produced the curves in Fig. 16 giving the reaction yield (R#2 or R#3) for that initial energy. Note that the energy dependences of the yields for R#2 and R#3 have the same general form as the proportionality curves of fast and tail decay components in Fig. 5.

Before leaving this topic, it is worthwhile to try to connect the results with the approximate treatment by Murray and Meyer of competing bimolecular exciton formation and defect trapping in a line track [35]. They postulated a system in which the free electrons and holes were created pairwise in linear number density  $n = n_h = n_e$  along a line of deposition. They considered "... that the electron can suffer two events, either recombining with a hole in the wake of the incident particle, or trapping at an unspecified site in the lattice", the latter according to a first-order trapping rate  $Kn$ . The productive bimolecular rate of electron-hole recombination to form the excitons that they suggested were responsible for  $Tl^{+*}$  emission can be written as the second order term  $Bn^2$ . The productive rate divided by the sum of all rates defined a yield written as

$$Y = \frac{Bn^2}{Kn + Bn^2} = \frac{\alpha n}{1 + \alpha n} \quad (9)$$

where  $\alpha = B/K$ . The expression on the right-hand side of this equation is the Murray-Meyer statement of expected radiative yield in this system. This describes a yield decreasing as the excitation number  $n$  decreases (in an assumed line deposition). The expression starts from

near zero at small  $n$ , rises at first quadratically, and approaches a saturating constant value of unity at large  $n$ . It does not turn down at large  $n$ , but saturates at unity because Murray and Meyer did not include either 2<sup>nd</sup> order (dipole-dipole) or 3<sup>rd</sup> order (Auger) nonlinear quenching. Eq. 9 is plotted in Fig. 15 with the dashed black curve, and its saturation asymptote with a solid grey line.

As noted above (and as well by Murray and Meyer [35]), this simple formula can give only a qualitative illustration of what goes on in a real particle track. For one reason, as we have seen in Fig. 6 and the surrounding discussion, roughly 90% of the electrons and holes are separated by hot electron diffusion and are trapped or self-trapped in different radial zones early in the pulse evolution [14, 37]. There are important electric field effects and trapping at play in their eventual recombination. As we have already noted, there are also nonlinear quenching terms not included in the Murray-Meyer formula. A solution of the full model description of transport, trapping, and recombination is necessary to make quantitative predictions of the light yield versus particle energy, i.e. results such as are shown in Fig. 5(b). Nevertheless, comparison of the Murray-Meyer curve and the reaction #2 curve in Fig. 15 reveals considerable similarity. This confirms that fundamentally, reaction #2 is bimolecular in excitation density when sufficient time is allowed for transport and recombination of dispersed trapped-carrier populations. The main linear trapping channel that competes with R#2 in the Murray-Meyer sense is actually STH capture on  $Tl^+$  to make  $Tl^{++}$ . Although this trapped-hole species will later produce light in R#3, it is a dark defect trap with respect to the "fast" scintillation of R#2. Electron trapping on deep defects in this model is also a competitor with R#2, but on a smaller scale than linear hole trapping to form  $Tl^{++}$ , simply because the concentration of  $Tl^+$  dopant exceeds defect concentration in most cases.

## VII. THE MATERIAL INPUT PARAMETERS

As described in Ref. [14], the model of scintillation that we have constructed tries to take into account the important physical processes of carrier generation, transport, recombination, nonlinear quenching, and capture on dopants and defects that seem logically required for physical description of the events in a particle track from which light yield and proportionality are determined. The number of material parameters necessary to specify those terms in a system of equations for free and trapped electrons, holes, and excitons is large, as was enumerated in Tables I and III of Ref. [14] for undoped and Tl-doped CsI. The good news about this circumstance is that for a model to yield information about effects caused by variation of material composition (concentration and species of doping, co-doping, defects, ...) the coefficients and rate constants of all those components should be

in the model or no specific information on material engineering by their variation can be obtained. The bad news is that good values for all of the parameters must be supplied whenever a new material system is modeled. There is a time investment for each new material. Over time, a library of tested parameter sets for important scintillator systems of interest should be built up. We believe that the material input parameters for CsI and CsI:Tl are approaching a reasonably well-tested status by virtue of the fitting and predictions of pulse shapes, energy dependence, absolute light yield, and proportionality (both total and by decay component) in the present work, evolving from the initial set in Ref. [14]. Undoubtedly there will be some further refinement of the material parameter values following direct experimental measurements and theoretical work in the future. But over time, validated parameter sets for a number of important scintillator systems should emerge from continuing work on CsI:Tl, and then on other materials as well.

Table I lists the parameters of CsI, all of which except for the deep defect trapping rate constant  $K_{1e}$  have remained unchanged in the present work relative to the values used for the calculation of proportionality and light yield in undoped CsI at 295 K in Ref. [14]. Note that the material parameters of undoped CsI are also used to describe the host when modeling CsI:Tl.

Table II lists the additional parameters needed to model CsI:Tl (0.06-0.08%), some of which did change in the process of fitting the wider array of data (i.e. pulse shape) in the present paper. The modeling in this study was done with the rate constant  $S_{1e}$  (for electron capture rate to form  $Tl^0$ ) at the value measured for nominal 0.08 mole % Tl in CsI [25], the same as the CsI:Tl fitted in Ref. [14]. Although the sample measured by Syntfeld-Kazuch et al [12, 13] contained 0.06% mole % Tl, we are not sure that falls outside the uncertainty of nominal 0.08% estimated from weight % Tl in the melt for the sample used in the picosecond measurements of  $S_{1e}$  [25].

When listing the Eqs. (1-7) in this paper, we introduced the "free electron fraction",  $f_e = U_{et}/S_{1e}$ , of  $Tl^0$  that are ionized in equilibrium, so that the free-electron values of  $D_e$ ,  $\mu_e$ , and  $K_{1e}$  could be used in Eqs. (4-6) rather than define new parameters  $D_{et}$ ,  $\mu_{et}$ , and  $K_{1et}$  scaled by the same factor as done in Ref. [14]. The defect trapping rate constant  $K_{1e}$  is proportional to the concentration of the responsible deep defects, which is sample dependent. Thus a determination of  $K_{1e}$  was made in this work from fitting the decay curve of the CsI:Tl (0.06%) sample studied by Syntfeld-Kazuch et al [12].

All of the changes in parameter values relative to Ref. [14] can be considered small or modest except the two bimolecular rate constants involving thallium:  $B_{et}$  for capture of STH on  $Tl^0$ , and  $B_{tt}$  ( $= B_{tt}^0 f_e$ ) for capture of an electron released from  $Tl^0$  on  $Tl^{++}$ , including the effect of release and recapture. The 1<sup>st</sup>-order capture rate constants that had not been directly measured were estimated in Ref. [14] as the product of a cross section,



TABLE I. Parameters used for the host parameters in the CsI:Tl model of the present work. Except for the deep defect trapping rate constant  $K_{1e}$  discussed in text, all parameters in this list are the same as used for the calculation of proportionality and light yield in undoped CsI at 295 K in Ref. [14]. In Table I of Ref. [14], literature references for the values were listed where available and otherwise comments on estimation methods were listed and explained in the text. See Ref. [14] for definitions of the parameters.

Parameter	Value	Units
$r_{track}$	3	nm
$\beta E_{gap}$	8.9	(eV/e-h) $_{avg}$
$\epsilon_0$	5.65	N/A
$\mu_e$	8	cm <sup>2</sup> /Vs
$D_e$	0.2	cm <sup>2</sup> /s
$\mu_h$	10 <sup>-4</sup>	cm <sup>2</sup> /Vs
$D_h$	2.6 x 10 <sup>-6</sup>	cm <sup>2</sup> /s
$D_E$	2.6 x 10 <sup>-6</sup>	cm <sup>2</sup> /s
$B(t > \tau_{hot})$	2.5 x 10 <sup>-7</sup>	cm <sup>3</sup> /s
$K_3$	4.5 x 10 <sup>-29</sup>	cm <sup>6</sup> /s
$K_{2E}$	0.8 x 10 <sup>-15</sup>	t <sup>-1/2</sup> cm <sup>3</sup> s <sup>-1/2</sup>
$R_{1E}$	6.7 x 10 <sup>6</sup>	s <sup>-1</sup>
$K_{1E}$	6 x 10 <sup>7</sup>	s <sup>-1</sup>
$\tau_{hot}$	4	ps
$r_{hot}$ (peak)	50	nm
$D_e(t < \tau_{hot})$	3.1	cm <sup>2</sup> /s
$S_{1e}$	0	s <sup>-1</sup>
$S_{1h}$	0	s <sup>-1</sup>
$S_{1E}$	0	s <sup>-1</sup>
$G_E(r = 0)$	0	cm <sup>-3</sup>
$K_{1e}$	2.7 x 10 <sup>10</sup>	s <sup>-1</sup>
$K_{1h}$	10 <sup>-5</sup> K <sub>1e</sub>	s <sup>-1</sup>
$E_i(norm)$	200	keV

TABLE II. Additional rate constants and transport parameters used in Eqs. (4-6) when modeling CsI:Tl (0.06%) at 295 K in the present work.  $S_{1e}$  is the value measured on CsI:Tl (nominal 0.08 mole %) [25]. See Ref. [14] for definitions of the parameters.

Parameter	Value	Units
$S_{1e}$	3.3 x 10 <sup>11</sup>	s <sup>-1</sup>
$S_{1h}$	5.0 x 10 <sup>6</sup>	s <sup>-1</sup>
$S_{1E}$	5.0 x 10 <sup>6</sup>	s <sup>-1</sup>
[Tl]	0.06	mole % in sample
$R_{1Et}$	1.7 x 10 <sup>6</sup>	s <sup>-1</sup>
$U_{Et}$	5.4 x 10 <sup>5</sup>	s <sup>-1</sup>
$B_{tt}$	2.5 x 10 <sup>-7</sup>	cm <sup>3</sup> /s
$B_{et}$	1.3 x 10 <sup>-10</sup>	cm <sup>3</sup> /s
$B_{ht}$	2.5 x 10 <sup>-7</sup>	cm <sup>3</sup> /s
$K_{2Et}$	1.7 x 10 <sup>-15</sup>	t <sup>-1/2</sup> cm <sup>3</sup> s <sup>-1/2</sup>

the concentration of the capturing defect, and the mean velocity of approach of the mobile carrier. When the approaching mobile carrier is a self-trapped hole, the velocity of approach is quite low, governed by the STH hopping rate. For capture on neutral traps (including substitutional Tl<sup>+</sup> in the CsI lattice), a geometrical cross

section can usually be assumed without large error. In this way, the value for  $S_{1h}$ , the first-order rate constant for capture of STH on Tl<sup>+</sup>, was estimated. For the 2<sup>nd</sup>-order capture of STH on Tl<sup>0</sup> governed by  $B_{et}$ , the cross section was assumed to be the same as found from ps absorption measurements of  $STH + e \rightarrow STE$ . During fitting of pulse shape in the present work, the STH population was found to be vanishing too quickly to support the observed rise time to peak. The need for a reduced value of  $B_{et}$  became clear, and there was recognition that the estimated value should have taken into account the low velocity of the approaching carrier (STH) in the case of  $STH + Tl^0 \rightarrow Tl^{+*}$ . This is the largest correction in Table II. Because the  $B_{et}n_{et}n_h$  rate term and the  $S_{1h}n_h$  rate term divide the available STH population as discussed earlier, reduction in the value of  $B_{et}$  required a balancing decrease in the value of  $S_{1h}$ , returning it close to the value of  $S_{1h}$  originally estimated in Ref. [14]. Mainly as a result of the decrease in  $S_{1h}$ , the self-trapped holes diffuse to larger radius before being nearly immobilized as a cylindrical positive charge of Tl<sup>++</sup>. One can compare the ~18 nm peak of the  $rn_{ht}$  distribution at 1  $\mu$ s in Fig. 9(d) of the present work to the ~4 nm peak of  $rn_{ht}$  at 1  $\mu$ s in Fig. 10(b) of Ref. [14]. This comparison is not perfect because the plot in Ref. [14] was for 10 $\times$  lower excitation density. In the similar comparison of  $rn_{et}$  at 1  $\mu$ s in Fig. 9(d) of this work with Fig. 9(b) of Ref. [14], the 4 nm peak of  $rn_{et}$  in the earlier work is no longer seen in the corresponding 1  $\mu$ s distribution of the present work. This can be attributed mainly to the revised smaller  $S_{1h}$  hole-capture parameter causing a more diffuse distribution of Tl<sup>++</sup> ( $n_{ht}$ ), which is less effective in attracting electrons to trap nearby as Tl<sup>0</sup> ( $n_{et}$ ).

The fitting of pulse shape in the present work required a significant increase in the value of  $B_{tt}$  relative to the estimate of this 2<sup>nd</sup>-order rate constant made in Ref. [14]. This underscores a conclusion we reached in this study, that fitting the proportionality alone can be fairly forgiving on some of the parameter choices. Fitting additional data with more structure, such as multiple rise and decay components of the pulse shape, can be used to refine parameters before undertaking calculation of proportionality, as done in the present study.

## VIII. CONCLUSIONS

Recent experiments on the scintillation response of CsI:Tl [12, 13] have shown that (1) there are three main decay times of about 730 ns, 3  $\mu$ s, and 16  $\mu$ s, i.e. one more principal decay component than had been previously reported; (2) for the sample studied, the 16  $\mu$ s component appears to exhibit exponential decay whereas the recombination kinetics widely regarded to be responsible for much of CsI:Tl scintillation comes from 2<sup>nd</sup> order electron-hole recombination on the activator; (3) the pulse shape depends on gamma ray energy; and (4) the proportionality curves of each decay component are dif-

ferent, with the energy dependent light yield of the 16  $\mu\text{s}$  component appearing to be anticorrelated with that of the 0.73  $\mu\text{s}$  component. These observations have been reasonably explained based on the model results presented.

This model of carrier transport and recombination takes into account the most important processes of hot and thermalized carrier diffusion, electric field transport, trapping, nonlinear quenching, and radiative recombination that can be expected to occur in particle tracks. Specifying the rates of such processes in a specific scintillator like CsI:Tl requires assembling a significant number of material parameter values measured in experiments independent of scintillation when possible, calculated theoretically in some cases, and refined by fitting to properties such as scintillation decay times in a few others. The assembled parameter set along with the equations in which they appear comprise an evolving model of scintillator response, in this study CsI:Tl.

The following conclusions are drawn:

(1) By examining population overlaps and reaction rates within the radial profile of the track, the 3- and 16-  $\mu\text{s}$  components were identified as the rate-limited and transport-limited phases of the same basic  $\text{Tl}^0 + \text{Tl}^{++}$  recombination.

(2) When a recombination process (e.g. 2<sup>nd</sup> order in this case) becomes transport limited, depending on electric field and concentration gradient between two separated reservoirs of carriers, the decay kinetics become 1<sup>st</sup> order consistent with apparent exponential decay of the 16  $\mu\text{s}$  tail component.

(3) The apparent exponential decay of the 730 ns fast component can be attributed mainly to the 575 ns 1st-order radiative decay of  $\text{Tl}^{+*}$ , but also perhaps to the finding that the 110 ns decay of the R#2 rate feeding the  $\text{Tl}^{+*}$  is itself transport limited and thus exponentially decaying.

(4) Results of the full model reproduced the main trend of energy-dependent pulse shape seen in experiment. Of the three major decay times, the 730 ns one is mainly due to  $(\text{STH} + \text{Tl}^0)$  R#2 in partial agreement with this attribution in the literature, but in addition the  $(\text{Tl}^0 + \text{Tl}^{++})$  R#3 reaction at small radius near the core contributes significantly in the time range at high excitation density ( $\sim$ low electron energy) and accounts for part of the energy dependence of pulse shape.

(5) Energy transport by STE to thallium activator can be no more than a minor contributor to any of the 3 main decay components at ordinary levels of Tl doping for scintillators.

(6) By analyzing the model results in terms of consumption of electrons and holes by two competing recombination reactions, second-order R#2 and first-order  $\text{Tl}^{++}$  formation preparatory for R#3, we could explain why the anticorrelation of the tail and fast decay components is to be expected at room temperature. The full model that fits the three decay components of scintillation also reproduces the main features of proportionality

for each of the separate decay components and a reasonable match of the total light yield at 662 keV.

(7) When integrating the light yield to 40  $\mu\text{s}$ , the calculated light output at 662 keV is 63 photons/keV, slightly higher than the reported value of 54 photons/keV [38]. But integration to such a long time is uncommon. In the more likely measurement conditions of 12  $\mu\text{s}$  and 4  $\mu\text{s}$  integrations the calculated yields are 57 and 48 photons/keV which bracket the reported value.

Work is underway to model similar experimental data sets on CsI at temperatures below and above room temperature, and to model the effects of changing concentration of activators and defects. As the collection of experimental data being compared to the model expands, we anticipate further refinement of parameter values for CsI:Tl. The model and its parameters for CsI and CsI:Tl should become more comprehensive and more tightly specified at the same time. Important applications of such a material-validated model will be to dissect the contributing processes in space and time as we have demonstrated in the present work, to gain insight on what controls various properties of the response, or to vary concentration and properties of activators, defects, and codopants while analyzing their contributions in ways that may not be open to direct experimental observation. Application of this basic model to other scintillator systems is underway [39–41]. A similar procedure of assembling material parameters from the literature as well as making estimates, followed by refining against pulse shape and other data, is being employed for each scintillator system.

The present model made certain assumptions in order to achieve relative computational simplicity. An important one is the assumption of cylindrical symmetry of track segments, rendering the problem effectively one-dimensional in the radial coordinate. Kinetic Monte Carlo methods used by Kerisit et al [23, 24, 42, 43] address local randomness of carrier distributions by simulating the individual diffusion and interactions of every electron and hole in the track starting from carrier creation distributions simulated by the NWEGRIM code [44, 45]. This avoids an assumption of local track symmetry but is also computationally demanding. Comparison of modeled scintillation response at energies of 400 keV and below currently addressed by both the Pacific Northwest National Laboratory (PNNL) Kinetic Monte Carlo method and the Wake Forest University (WFU) transport & rate equation method could answer questions on the effect of approximations such as cylindrical track that have enabled relatively fast simulations of scintillation response in the present work. Collaborative work of the WFU and PNNL groups is ongoing.

## ACKNOWLEDGMENTS

WFU acknowledges support from the US Department of Homeland Security, Domestic Nuclear De-

tection Office, DNDO-NSF-ARI Grant 2014-DN-077-ARI-077 and National Nuclear Security Administration (NNSA), Office of Defense Nuclear Nonproliferation Research and Development (DNN R&D) under Venture Contract LB15-V-GammaDetMater-PD2Jf through Lawrence Berkeley National Laboratory. This support does not constitute express or implied endorsement on the part of the Government. Partial support is also acknowledged from the Polish National Centre for Research

and Development under project "RaM-scaN", Grant No. PBS2/B2/11/2014 and by the European Union's VII-th Framework Programme for research, technological development and demonstration under "TAWARA" grant agreement No. 312713. The work is partially supported by the NATO multiyear Science for Peace Project NUKR.SFPP 984958 "New sensor materials and detectors for ionizing radiation detection."

- 
- [1] Pieter Dorenbos, "Fundamental Limitations in the Performance of  $Ce^{3+}$ ,  $Pr^{3+}$ , and  $Eu^{2+}$  Activated Scintillators," *IEEE Transactions on Nuclear Science* **57**, 1162–1167 (2010).
- [2] M. Moszyński, A. Syntfeld-Kazuch, L. Swiderski, M. Grodzicka, J. Iwanowska, P. Sibirzyński, and T. Szcześniak, "Energy resolution of scintillation detectors," *Nuclear Instruments and Methods in Physics Research Section A: Accelerators, Spectrometers, Detectors and Associated Equipment* **805**, 25–35 (2016).
- [3] Glenn F. Knoll, *Radiation Detection and Measurement*, 4th ed. (2011).
- [4] C.L. Melcher, "Scintillators for well logging applications," *Nuclear Instruments and Methods in Physics Research Section B: Beam Interactions with Materials and Atoms* **40-41**, 1214–1218 (1989).
- [5] Nerine J Cherepy, Steve A Payne, Benjamin W Sturm, Owen B Drury, Sean P. O'Neal, Peter A Thelin, Kanai S Shah, Rastgo Hawrami, Michael Momayezi, Brad Hurst, Arnold Burger, Brenden Wiggins, Pijush Bhattacharya, Lynn A Boatner, and Joanne O Ramey, "Instrument Development and Gamma Spectroscopy With Strontium Iodide," *IEEE Transactions on Nuclear Science* **60**, 955–958 (2013).
- [6] Paul Lecoq, "Development of new scintillators for medical applications," *Nuclear Instruments and Methods in Physics Research Section A: Accelerators, Spectrometers, Detectors and Associated Equipment* **809**, 130–139 (2016).
- [7] Maurizio Conti, "State of the art and challenges of time-of-flight PET," *Physica Medica* **25**, 1–11 (2009).
- [8] Paul Lecoq, Mikhael Korzhik, and Andrey Vasiliev, "Can Transient Phenomena Help Improving Time Resolution in Scintillators?" *IEEE Transactions on Nuclear Science* **61**, 229–234 (2014).
- [9] M. Moszynski, A Nassalski, A Syntfeld-Kazuch, L Swiderski, and T. Szczechniak, "Energy Resolution of Scintillation Detectors - New Observations," *IEEE Transactions on Nuclear Science* **55**, 1062–1068 (2008).
- [10] R. T. Williams, X. Lu, S. Gridin, P. Li, D. R. Onken, K. B. Ucer, A. Burger, and M. R. Mayhugh, "Information on Particle Track Structure Carried in Scintillation Pulse Shape? Present and Potential Applications," (2016), presented at International Conference on Optical, Opto-electronic, and Photonic Materials and Applications (ICOOPMA 2016), (unpublished).
- [11] R. T. Williams, Xinfu Lu, A. Syntfeld-Kazuch, L. Świderski, M. Moszyński, and A. V. Gektin, "Transport and rate equation modeling of experiments on proportionality of decay time components in CsI:TI," (2015), presented at IEEE Nuclear Science Symposium and Medical Imaging Conference (NSS-MIC), (unpublished).
- [12] A. Syntfeld-Kazuch, M. Moszynski, L. Swiderski, W Klamra, and A Nassalski, "Light Pulse Shape Dependence on  $\gamma$ -Ray Energy in CsI (TI)," *IEEE Transactions on Nuclear Science* **55**, 1246–1250 (2008).
- [13] Agnieszka Syntfeld-Kazuch, Lukasz Swiderski, Marek Moszynski, and Alexander V Gektin, "Non-proportionality components in doped CsI," in *2014 IEEE Nuclear Science Symposium and Medical Imaging Conference (NSS/MIC)*, X (IEEE, 2014) pp. 1–3.
- [14] Xinfu Lu, Qi Li, G. A. Bizarri, Kan Yang, M. R. Mayhugh, P. R. Menge, and R. T. Williams, "Coupled rate and transport equations modeling proportionality of light yield in high-energy electron tracks: CsI at 295 K and 100 K; CsI:TI at 295 K," *Physical Review B* **92**, 115207 (2015).
- [15] S. Agostinelli, "Geant4 - a simulation toolkit," *Nuclear Instruments and Methods in Physics Research Section A: Accelerators, Spectrometers, Detectors and Associated Equipment* **506**, 250–303 (2003).
- [16] Joel Q. Grim, K. B. Ucer, A. Burger, P. Bhattacharya, E. Tupitsyn, E. Rowe, V. M. Buliga, L. Trefilova, A. Gektin, G. a. Bizarri, W. W. Moses, and R. T. Williams, "Nonlinear quenching of densely excited states in wide-gap solids," *Physical Review B* **87**, 125117 (2013).
- [17] L. Swiderski, R. Marcinkowski, M. Szawlowski, M. Moszynski, W. Czarnacki, A. Syntfeld-Kazuch, T. Szczechniak, G. Pausch, C. Plettner, and K. Roemer, "Non-Proportionality of Electron Response and Energy Resolution of Compton Electrons in Scintillators," *IEEE Transactions on Nuclear Science* **59**, 222–229 (2012).
- [18] M. Moszyński, M. Balcerzyk, W. Czarnacki, A. Nassalski, T. Szcześniak, H. Kraus, V.B. Mikhailik, and I.M. Solskii, "Characterization of CaWO4 scintillator at room and liquid nitrogen temperatures," *Nuclear Instruments and Methods in Physics Research Section A: Accelerators, Spectrometers, Detectors and Associated Equipment* **553**, 578–591 (2005).
- [19] M. Grodzicka, M. Moszyński, T. Szcześniak, W Czarnacki, M. Szawlowski, L. Świderski, L. Kaźmierczak, and K. Grodzicki, "Characterization of CsI:TI at a wide temperature range (-40C to +22C)," *Nuclear Instruments and Methods in Physics Research Section A: Accelerators, Spectrometers, Detectors and Associated Equipment* **707**, 73–79 (2013).
- [20] John D. Valentine, William W. Moses, Stephen E. Derenzo, David K Wehe, and Glenn F Knoll, "Temperature dependence of CsI(Tl) gamma-ray excited scintilla-

- tion characteristics,” *Nuclear Instruments and Methods in Physics Research Section A: Accelerators, Spectrometers, Detectors and Associated Equipment* **325**, 147–157 (1993).
- [21] M.M. Hamada, F.E. Costa, M.C.C. Pereira, and S. Kubota, “Dependence of scintillation characteristics in the CsI(Tl) crystal on  $Tl^+$  concentrations under electron and alpha particles excitations,” *IEEE Transactions on Nuclear Science* **48**, 1148–1153 (2001).
- [22] H. Dietrich, A. Purdy, R. Murray, and R. Williams, “Kinetics of Self-Trapped Holes in Alkali-Halide Crystals: Experiments in NaI(Tl) and KI(Tl),” *Physical Review B* **8**, 5894–5901 (1973).
- [23] Sebastien Kerisit, Kevin M. Rosso, and Bret D. Cannon, “Kinetic Monte Carlo Model of Scintillation Mechanisms in CsI and CsI(Tl),” *IEEE Transactions on Nuclear Science* **55**, 1251–1258 (2008).
- [24] Zhiguo Wang, YuLong Xie, Luke W. Campbell, Fei Gao, and Sebastien Kerisit, “Monte Carlo simulations of electron thermalization in alkali iodide and alkaline-earth fluoride scintillators,” *Journal of Applied Physics* **112**, 014906 (2012).
- [25] K. B. Ucer, G. Bizarri, A. Burger, A. Gektin, L. Trefilova, and R. T. Williams, “Electron thermalization and trapping rates in pure and doped alkali and alkaline-earth iodide crystals studied by picosecond optical absorption,” *Physical Review B* **89**, 165112 (2014).
- [26] A. Belsky, C. Dujardin, A. Gektin, S. Gridin, I. Iskandarova, A. Scherbinin, N. Shiran, and A. Vasil’ev, “Activator levels in CsI crystals doped with  $Tl^+$  and  $In^+$  ions,” (2015), presented at 9th International Conference on Luminescent Detectors and Transformers of Ionizing Radiation (LUMDETR 2015), (unpublished).
- [27] V. Yakovlev, L. Trefilova, A. Meleshko, V. Alekseev, and N. Kosinov, “Charge transfer processes in CsI:Tl using near-UV light,” *Journal of Luminescence* **155**, 79–83 (2014).
- [28] M. H. Du, “Chemical trends of electronic and optical properties of  $ns^2$  ions in halides,” *Journal of Materials Chemistry C* **2**, 4784 (2014).
- [29] V. Nagirnyi, A. Stolovich, S. Zazubovich, V. Zepelin, E. Mihokova, E. Nikl, G. P. Pazzi, and L. Salvini, “Peculiarities of the triplet relaxed excited-state structure and luminescence of a CsI:Tl crystal,” *Journal of Physics: Condensed Matter* **7**, 3637–3653 (1995).
- [30] R. Gwin and R. Murray, “Scintillation Process in CsI(Tl). II. Emission Spectra and the Possible Role of Self-Trapped Holes,” *Physical Review* **131**, 508–512 (1963).
- [31] Shunji Nagata, Koji Fujiwara, and Hitoshi Nishimura, “Dynamical aspects of excitons in NaI,” *Journal of Luminescence* **47**, 147–157 (1990).
- [32] H. Nishimura, M. Sakata, T. Tsujimoto, and M. Nakayama, “Origin of the 4.1 eV luminescence in pure CsI scintillator,” *Physical Review B* **51**, 2167–2172 (1995).
- [33] Lukasz Swiderski, Marek Moszynski, Antoni Nassalski, Agnieszka Syntfeld-Kazuch, Wieslaw Czarnacki, Wlodzimierz Klamra, and Valentin a. Kozlov, “Scintillation Properties of Undoped CsI and CsI Doped With CsBr,” *IEEE Transactions on Nuclear Science* **55**, 1241–1245 (2008).
- [34] Lukasz Swiderski, Marek Moszynski, Agnieszka Syntfeld-Kazuch, Marek Szawlowski, and Tomasz Szczesniak, “Measuring the scintillation decay time for different energy depositions in NaI:Tl, LSO:Ce and CeBr<sub>3</sub> scintillators,” *Nuclear Instruments and Methods in Physics Research Section A: Accelerators, Spectrometers, Detectors and Associated Equipment* **749**, 68–73 (2014).
- [35] R. Murray and A. Meyer, “Scintillation Response of Activated Inorganic Crystals to Various Charged Particles,” *Physical Review* **122**, 815–826 (1961).
- [36] S. Gridin, A. Belsky, C. Dujardin, A. Gektin, N. Shiran, and A. Vasil’ev, “Kinetic Model of Energy Relaxation in CsI:A (A = Tl and In) Scintillators,” *The Journal of Physical Chemistry C* **119**, 20578–20590 (2015).
- [37] Zhiguo Wang, YuLong Xie, Bret D. Cannon, Luke W. Campbell, Fei Gao, and Sebastien Kerisit, “Computer simulation of electron thermalization in CsI and CsI(Tl),” *Journal of Applied Physics* **110**, 064903 (2011).
- [38] “<http://www.crystals.saint-gobain.com>,”.
- [39] M. R. Mayhugh, Xinfu Lu, S. Gridin, S.B. Donald, C.L. Melcher, and R. T. Williams, “From CsI:Tl to YAP:Ce - A Modeling Study of the Material Parameter Sensitivity of Proportionality,” (2016), presented at Symposium on Radiation Monitoring and Applications (SORMA 2016), (unpublished).
- [40] K. B. Ucer, Sergii Gridin, Peiyun Li, Xinfu Lu, R. T. Williams, M. R. Mayhugh, A. V. Gektin, Kan Yang, P. R. Menge, and G. A. Bizarri, “NaI and NaI:Tl picosecond spectroscopy and scintillation modeling,” (2016), presented at Symposium on Radiation Monitoring and Applications (SORMA 2016), (unpublished).
- [41] S. Gridin, X. Lu, P. Li, B. Ucer, R. Williams, K. Yang, and P. Menge, “LaBr<sub>3</sub> with Ce and Sr dopants: picosecond absorption spectroscopy and progress on track modeling,” (2016), presented at International Conference on Defects in Insulating Materials (ICDIM 2016), (unpublished).
- [42] Sebastien Kerisit, Kevin M. Rosso, Bret D. Cannon, Fei Gao, and YuLong Xie, “Computer simulation of the light yield nonlinearity of inorganic scintillators,” *Journal of Applied Physics* **105**, 114915 (2009).
- [43] Zhiguo Wang, Richard T. Williams, Joel Q. Grim, Fei Gao, and Sebastien Kerisit, “Kinetic Monte Carlo simulations of excitation density dependent scintillation in CsI and CsI(Tl),” *physica status solidi (b)* **250**, 1532–1540 (2013).
- [44] Fei Gao, Luke W. Campbell, Ram Devanathan, Yu-long Xie, L. Rene Corrales, Anthony J. Peurrung, and William J. Weber, “Monte Carlo method for simulating  $\gamma$ -ray interaction with materials: A case study on Si,” *Nuclear Instruments and Methods in Physics Research Section A: Accelerators, Spectrometers, Detectors and Associated Equipment* **579**, 292–296 (2007).
- [45] F. Gao, Y. Xie, S. Kerisit, L.W. Campbell, and W.J. Weber, “Yield, variance and spatial distribution of electron-hole pairs in CsI,” *Nuclear Instruments and Methods in Physics Research Section A: Accelerators, Spectrometers, Detectors and Associated Equipment* **652**, 564–567 (2011).